International Journal of Engineering Science 206 (2025) 104168

Contents lists available at ScienceDirect

International Journal of Engineering Science

journal homepage: www.elsevier.com/locate/ijengsci

On quasi-brittle static fracture analysis of micropolar plates via XFEM model

Meral Tuna [a], Patrizia Trovalusci [b,*], Nicholas Fantuzzi [a]

[a] Department of Civil, Chemical, Environmental and Materials Engineering, University of Bologna, Bologna, Italy
[b] Department of Structural and Geotechnical Engineering, Sapienza University of Rome, Rome, Italy

ARTICLE INFO

Keywords:
Cosserat
LEFM
XFEM
I-integral
Intensity factors

ABSTRACT

The main objective of this study is to implement extended finite element method (XFEM) to two-dimensional (2D) micropolar structures in order to extract basic fracture parameters required in linear elastic fracture mechanics (LEFM) in a computationally efficient manner, and thus to provide basis to explore the crack propagation phenomenon within this framework. The stress and couple-stress intensity factors (SIF and CSIF) are detected with the aid of interaction integral, *I-integral*, and compared with the ones in the literature for validation purposes while an engineering problem of practical importance; plate with an oblique edge crack, is investigated to demonstrate the applicability of the developed methodology. The approach presents considerable simplification in modeling process owing to ability of XFEM to treat discontinuities and singularities appeared in the cracked domains, and offers a new, and different perspective to available methods (e.g. phase field method and peridynamics), each with their own advantages and limitations, extended to deal with crack and its growth in micropolar structures.

1. Introduction

1.1. Background

The deteriorating effect of cracks in materials, particularly pronounced in brittle case (Gdoutos, 2006; Inglis, 1913), attracts many researchers to investigate the fracture characteristics of composites, which are notorious for being prone to flaws (Kachanov, 2022; Kachanov & Argatov, 2023; Kanaun et al., 2023; Kushch et al., 2009; Markov & Kanaun, 2014; Markov et al., 2024; Ponnusami et al., 2015). As such materials with comparable internal (e.g. size of heterogeneity) and external (e.g. sample dimension) length scales, calls for the consideration of size-effects through non-classical (non-local) theories (Capriz, 1989; Eringen, 1999; Gurtin, 1999; Kunin, 1984; Maugin, 1993; Mindlin, 1964), it is crucial to examine the fracture characteristics within this framework.

Since it is a common practice to use non-local models in pursuit of investigating the behavior of size-dependent structures (e.g. Barretta et al., 2024; Farajpour et al., 2020; Ghayesh & Farajpour, 2019; Karami et al., 2019; Stempin et al., 2023), micropolar theory of elasticity forms the basis of this work following its ability to account for the micro-rotation of individual material points by including internal length scales in the field equations (Altenbach & Eremeyev, 2012; Cosserat & Cosserat, 1909; Eringen, 1999; Nowacki, 1986). This theory belongs to a group of generalized (multifield) continua with additional degrees of freedom (DOFs) which integrates size

* Corresponding author.
E-mail addresses: meral.tunaeroglu@unibo.it (M. Tuna), patrizia.trovalusci@uniroma1.it (P. Trovalusci), nicholas.fantuzzi@unibo.it (N. Fantuzzi).

https://doi.org/10.1016/j.ijengsci.2024.104168
Received 24 June 2024; Received in revised form 3 October 2024; Accepted 19 October 2024
0020-7225/© 2024 Elsevier Ltd. All rights are reserved, including those for text and data mining, AI training, and similar technologies.

effects through non-standard kinematic (i.e. curvature) and work-conjugated dynamic (i.e. couple-stress) descriptors.

Although micropolar theory has been exploited widely to investigate the undamaged/uncracked state of materials with presence of particle rotations; as in ceramics, particulate, fibre-reinforced or granular composites (Colatosti et al., 2021; Forest & Sab, 1998; Jasiuk & Ostoja-Starzewski, 2004; Masiani & Trovalusci, 1996; Trovalusci & Masiani, 2003; Tuna & Trovalusci, 2020, 2021), the number of works that deals with fracture characteristics (damaged/cracked state) of such structures are somehow limited with the majority considering the case of stationary (non-propagating) cracks. Nonetheless, recently, the topic has started to gain a considerable attention, by specifically concentrating on the crack propagation phenomenon via extending methodologies such as phase field (Behera et al., 2024; Riad et al., 2022; Suh et al., 2020), and peridynamics (Chen et al., 2024; Diana et al., 2024; Guo et al., 2024; Lei et al., 2024; Wan et al., 2022; Zhou et al., 2023) to micropolar continuum. On the other hand, in spite of its potential and extensive application to domains with stationary cracks (detailed in the subsequent subsection), linear elastic fracture mechanics (LEFM) has not been exploited to explore the crack propagation phenomenon in micropolar structures. This can be attributed to;

(i) the absence of a numerically versatile approach offering the propagation phenomenon to be modeled in a computationally efficient manner,
(ii) the absence of a valid fracture criterion providing the propagation (kinking) angle forming the crack path,

while, in this study, we aimed at addressing the former (i) issue, which inherently contributes to the latter (ii) one, as discussed later.

1.2. Literature on micropolar/LEFM approach

The foundation of LEFM dates back to Griffth's study on scratched glass specimens (Griffith, 1921), and following the landmark works of Barenblatt, 1962, Cherepanov 1967, Eshelby, 1974, Irwin, 1948, 1957, 1968, Orowan 1949, Rice, 1968, Stern et al. 1976, it has gained a considerable attention. The damage characteristics of a brittle/quasi-brittle structure is described by means of basic fracture parameters, such as crack-tip fields, energy release rate (ERR), stress intensity factors (SIFs), and crack mouth opening displacement by treating any loading state as a combination of Mode I (opening), Mode II (shearing) and Mode III (tearing) cases.

In literature, the first study that associates LEFM with micropolar continua was conducted by Sternberg & Muki, 1967 in the framework of couple-stress (constrained micropolar) theory, and later generalized for the micropolar solids by Atkinson & Leppington 1977. In these studies, non-locality was proved to reduce the effect of cracks as stress concentrators by showing the decreasing trend of energy release rate (ERR), while the stress and couple stress fields were demonstrated to be asymptotic as in classical elastic case, and a new physical quantity, called as couple stress intensity factor (CSIF), was introduced to describe the amplitude of couple stress singularity at the crack tip. Similar observations were also made by Paul & Sridharan 1981, in which the stiffening effect of increased micropolarity was highlighted by tabulating the values of ERR, SIF, CSIF and crack opening displacement for various material properties. These pioneering studies are followed by the works of Jaric (1990), Lubarda & Markenscoff (2003), Mühlhaus & Pasternak (2002), Niktitin & Zubov (1998), Pucci & Saccomandi (1990), on the derivation of the conservation integrals (e.g. J-integral and I-integral), which allows adoption of remote quantities in prediction of fracture parameters. Meanwhile, Garajeu & Soós (2003) and Diegele et al. (2004) independently obtained the near crack-tip stress/couple-stress and displacement/rotation fields in an explicit manner under combined loading conditions. The latter study also conducted standard finite element method (FEM) to reveal the influence of non-locality on the trend of SIFs and CSIF, a point that was highlighted later again in the parametric study by Li & Lee (2009). The derivation of analytical expressions and conversation integrals has promoted the use of numerical approaches in studying the correspondence between micropolarity and the basic fracture parameters (Atroshchenko & Bordas 2015; Kapiturova et al. 2016; Yu et al. 2014). For instance; Yu et al. (2014) has successfully implemented the interaction integral concept (I-integral) into enriched FE model and has generalized the formulation for non-homogeneous case. The modeling process is eased with the aid of Heaviside-step function that permits finite elements to be cut by the crack, nevertheless the discretization around the crack tip still needed to be adjusted and refined for high precision. Similarly, Atroshchenko & Bordas (2015) generalized boundary element method (BEM) to micropolar solids, and obtained fracture parameters in agreement with the literature with the expense of gradually refining the elements towards the crack tip. All these efforts have paved the way to works that concentrated on the fracture analysis of actual structures established in the framework of micropolar theory, such as planar lattices (Berkache et al. 2022) and fiber-reinforced biocomposites (Dong et al., 2022).

1.3. Motivation

The strong correspondence between the level of non-locality (micropolarity) and the basic fracture parameters: SIFs, CSIF, ERR, that must be determined to identify the state of the structure considering brittle case, is evident. With the motivation to have a numerical approach allowing these parameters to be obtained in a computationally efficient manner, the Authors have implemented extended finite element method (XFEM) to micropolar continuum, which forms the basis to analyze the damage process within the framework of LEFM. The formulation is presented considering two-dimensional, homogeneous linear-elastic, isotropic materials that follows plane strain assumption, and linearized kinematical framework. As the work is focused on brittle/quasi-brittle static fracture analysis, dynamical effects and localization phenomenon are beyond the scope, hence not included herein. The XFEM, which was initially established by Belytschko & Black (1999), Daux et al. (2000), Dolbow (1999), Moes, Dolbow & Belytschko (1999), and utilized in modeling the crack growth (Huang et al., 2003; Sukumar & Prevost, 2003) for classical materials, allows the finite element mesh to be completely independent of the discontinuities and singularities appeared in the domain with the aid of enrichment

functions. Following its development, the accuracy and convergence rate of the methodology has been constantly improved by proposing new enrichment types, blending strategies, and preconditioners (Béchet et al., 2005; Chessa et al., 2003; Deng et al., 2023; Fries 2008; Gracie et al., 2008; Gupta et al., 2013; Laborde et al., 2005; Tarancon et al., 2009; Tian & Wen 2015; Wen et al., 2023), via which the solution of many problems including domains with multiple cracks, delamination, dislocation, multi-materials, and so on, have been investigated (Belytschko et al., 2009; Benvenuti et al., 2016; Chroni et al., 2024; Deng et al., 2022; Fries & Belytschko 2010). In the present study, micropolar/XFEM model is achieved with locally enriching the nodes located in the influence domain of discontinuity and singularity through Heaviside-step and crack-tip branch functions considering both translational and micro-rotational DOFs, similar to Kapiturova et al., 2016. Keeping in mind that, the first noteworthy attempt in this sense (combining XFEM with micropolar theory) was made by Kapiturova et al., 2016, the proposed methodology did not account for distinguishing the contributions of Mode I and Mode II and the contributions of stress and couple-stress intensity factors from each other. The trend of energy release rate reported only for Mode I case seems to have an increasing trend with non-locality, which is in disagreement with the literature (Atkinson & Leppington, 1977; Paul & Sridharan, 1981).

Accordingly, in Section 2, the basic field equations of micropolar theory and generalized LEFM are revisited. The *J* and *I-integrals*, required for extraction of the fracture parameters within micropolar solids are re-derived and the corresponding micropolar/XFEM model is presented. In Section 3, the in-house code (micropolar/XFEM model), that is built in the environment of Wolfram Mathematica©, is validated through various benchmark problems under Mode I and Mode II, and a parametric study is performed on an uniaxially loaded finite domain with an inclined edge crack to examine the effect of non-locality on mixed mode (Mode I + Mode II) case. In Section 4, the potential of micropolar/XFEM model for brittle fracture analysis of size-dependent plates is discussed alongside with capability and limitations of other available approaches. Finally, in Section 5, the study is summarized with suggesting future developments.

2. Micropolar theory of elasticity

In this section, the field equations of the two-dimensional (2D) micropolar medium is presented under plane strain assumption by using Cartesian coordinate system Ox_1x_2 as reference since it is a very common practice to model a thick plate with no (or negligible) strain along the longitudinal axis as a 2D body under plane strain assumption, whether it is intact or defected. Then, the crack-tip asymptotic fields that are derived within the framework of linear elastic fracture mechanics (LEFM) (Diegele et al., 2004 and Garajeu & Soós, 2003) are used to obtain the explicit expressions of path-independent *J* and *I-integrals*, required for extraction of stress intensity (SIF) and couple-stress intensity (CSIF) factors. Finally, extended finite element method (XFEM) is implemented to micropolar structures considering both Heaviside and crack-tip enrichment functions, which eliminates the need to have a mesh conforming with crack geometry. In the formulation, adopting the deformation fields and constitutive relations that are in line with plane strain state allows us to perform validation studies by comparing our results with the ones available in literature all of which are derived based on plane strain assumption within the linearized kinematical framework by considering the domain as linear-elastic, homogeneous and isotropic. For calculations an in-house code is developed using Wolfram Mathematica ©.

2.1. Field equations

In case of micropolar theory of elasticity, the material domain includes additional micro-rotational DOFs, leading to the incorporation of new strain and work-conjugated stress measures, known as curvature, $\boldsymbol{\chi}$, and couple-stress, $\boldsymbol{\mu}$, whereas the classical strain and stress tensors, $\boldsymbol{\varepsilon}$, $\boldsymbol{\sigma}$, are not symmetrical.

For planar case, u_1, u_2 and ϕ_3 are the independent variables representing the displacement components along axial, x_1, and vertical, x_2, directions and micro-rotation about x_3 axis, respectively. Accordingly, following kinematic relations are recovered under linearized framework;

$$\begin{aligned}
&\varepsilon_{ij} = u_{j,i} - \epsilon_{kij}\phi_k, \quad \chi_{ij} = \phi_{j,i} \\
&\text{In2D}: \\
&\varepsilon_{11} = u_{1,1}, \qquad \varepsilon_{22} = u_{2,2} \\
&\varepsilon_{12} = u_{2,1} - \phi_3, \quad \varepsilon_{21} = u_{1,2} + \phi_3, \\
&\chi_{13} = \phi_{3,1}, \qquad \chi_{23} = \phi_{3,2}
\end{aligned} \tag{1}$$

where comma indicating the partial derivative operation, and ϵ is the permutation symbol. In the special case, where micro-rotations are constrained to follow macro-rotations; $\phi_k = 1/2\epsilon_{kmn}u_{n,m}$, the classical kinematic relations; $\varepsilon_{ij} = 1/2\left(u_{i,j} + u_{j,i}\right)$, are recovered, resulting in couple-stress theory (Sokolowski, 1972). As for the balance consideration, following equations are obtained in the absence of body loads:

$$\begin{aligned}
&\sigma_{ji,j} = 0, \quad \mu_{ji,j} + \epsilon_{ijk}\sigma_{jk} = 0 \\
&\text{In2D}: \\
&\sigma_{11,1} + \sigma_{21,2} = 0, \\
&\sigma_{12,1} + \sigma_{22,2} = 0, \\
&\sigma_{12} - \sigma_{21} + \mu_{13,1} + \mu_{23,2} = 0
\end{aligned} \tag{2}$$

Finally, for a linear elastic isotropic solid, the relations between strain and stress, curvature and couple-stress fields are:

$$\begin{aligned}\sigma_{ij} &= \lambda\delta_{ij}\varepsilon_{kk} + (\mu+\kappa)\varepsilon_{ij} + (\mu-\kappa)\varepsilon_{ji}\\ \mu_{ij} &= \beta\delta_{ij}\chi_{kk} + (\gamma+\varepsilon)\chi_{ij} + (\gamma-\varepsilon)\chi_{ji}\end{aligned} \tag{3}$$

Here κ, γ, β and ε are micropolar parameters, whereas μ and λ are the classical Lame's constants that can be used to represent Young's modulus, E, and Poisson's ratio, ν:

$$E = \frac{\mu(3\lambda+2\mu)}{\lambda+2\mu}, \quad \nu = \frac{\lambda}{2(\lambda+\mu)} \tag{4}$$

When the general form of the constitutive equations, Eq. (3), is simplified for the case of plane-strain, we have:

$$\begin{Bmatrix}\sigma_{11}\\ \sigma_{22}\\ \sigma_{12}\\ \sigma_{21}\end{Bmatrix} = \underbrace{\begin{bmatrix}2\mu+\lambda & \lambda & 0 & 0\\ \lambda & 2\mu+\lambda & 0 & 0\\ 0 & 0 & \mu+\kappa & \mu-\kappa\\ 0 & 0 & \mu-\kappa & \mu+\kappa\end{bmatrix}}_{\mathbf{D}^e}\begin{Bmatrix}\varepsilon_{11}\\ \varepsilon_{22}\\ \varepsilon_{12}\\ \varepsilon_{21}\end{Bmatrix}, \quad \begin{Bmatrix}\mu_{13}\\ \mu_{23}\end{Bmatrix} = \underbrace{\begin{bmatrix}\gamma & 0\\ 0 & \gamma\end{bmatrix}}_{\mathbf{D}^\chi}\begin{Bmatrix}\chi_{13}\\ \chi_{23}\end{Bmatrix} \tag{5}$$

Here $(\gamma+\varepsilon)$ appeared in Eq. (3) is considered as a single parameter symbolized with γ. Hence, the contribution of size effects and relative rotations are included through γ, κ parameters which can alternatively represented in terms of internal characteristic length, l_c, and coupling number, N(Lakes, 1995):

$$l_c^2 = \frac{\gamma}{4\mu}, \quad l_c > 0 \quad \& \quad N^2 = \frac{\kappa}{\mu+\kappa}, \quad N \in [0,1] \tag{6}$$

The latter limit for N indicates couple-stress theory, while in case the values of N and l_c approach to the zero, the micropolar model reduces to Cauchy for the case of isotropy (Trovalusci & Masiani, 1999).

2.2. Linear elastic fracture mechanics

2.2.1. Crack-tip asymptotic fields

For a micropolar elastic medium with a pre-existing crack, the near tip stress and couple-stress fields, that are derived by Diegele et al., 2004 and Garajeu & Soós, 2003, takes the following form considering a local Cartesian coordinate system. Here the symbol tilde appears over the stress and couple-stress fields refers to the components in local coordinates, $\tilde{x}_1, \tilde{x}_2$, while the x_1, x_2 are global coordinates, and the angle in-between is symbolized by α as shown in Fig. 1.

$$\begin{Bmatrix}\tilde{\sigma}_{11}\\ \tilde{\sigma}_{22}\\ \tilde{\sigma}_{12}\\ \tilde{\sigma}_{21}\end{Bmatrix} = \frac{K_I}{\sqrt{2\pi r}}\begin{Bmatrix}\frac{S}{4}\left(3\mathrm{Cos}\frac{\theta}{2}+\mathrm{Cos}\frac{5\theta}{2}\right)\\ \frac{S}{4}\left(\mathrm{Cos}\frac{\theta}{2}-\mathrm{Cos}\frac{5\theta}{2}\right)+\mathrm{Cos}\frac{\theta}{2}\\ \frac{S}{4}\left(3\mathrm{Sin}\frac{\theta}{2}+\mathrm{Sin}\frac{5\theta}{2}\right)-\mathrm{Sin}\frac{\theta}{2}\\ \frac{S}{4}\left(\mathrm{Sin}\frac{5\theta}{2}-\mathrm{Sin}\frac{\theta}{2}\right)\end{Bmatrix} + \frac{K_{II}}{\sqrt{2\pi r}}\begin{Bmatrix}-\frac{S}{4}\left(3\mathrm{Sin}\frac{\theta}{2}+\mathrm{Sin}\frac{5\theta}{2}\right)-\mathrm{Sin}\frac{\theta}{2}\\ \frac{S}{4}\left(\mathrm{Sin}\frac{5\theta}{2}-\mathrm{Sin}\frac{\theta}{2}\right)\\ \frac{S}{4}\left(3\mathrm{Cos}\frac{\theta}{2}+\mathrm{Cos}\frac{5\theta}{2}\right)\\ \frac{S}{4}\left(\mathrm{Cos}\frac{5\theta}{2}-\mathrm{Cos}\frac{\theta}{2}\right)+\mathrm{Cos}\frac{\theta}{2}\end{Bmatrix}+\ldots$$

$$\begin{Bmatrix}\tilde{\mu}_{13}\\ \tilde{\mu}_{23}\end{Bmatrix} = \frac{L_I}{\sqrt{2\pi r}}\begin{Bmatrix}-\mathrm{Sin}\frac{\theta}{2}\\ \mathrm{Cos}\frac{\theta}{2}\end{Bmatrix} + l_{II}\begin{Bmatrix}1\\ 0\end{Bmatrix} \tag{7}$$

where

$$S = \frac{1-2(1-\nu)N^2}{1+2(1-\nu)N^2} \tag{8}$$

with r and θ being the radial distance from crack tip and counter-clockwise angle from $\tilde{x}_1$ axis, respectively. Here the SIFs; K_I, K_{II}, CSIF; L_I, and constant couple-stress factor, l_{II}, are defined following the definition in Diegele et al., 2004 and Yu et al., 2014:

$$\begin{aligned}K_I &:= \lim_{r\to 0}\left\{\sqrt{2\pi r}\,\tilde{\sigma}_{22}(r,\theta)|_{\theta=0}\right\}, \quad K_{II} := \lim_{r\to 0}\left\{\sqrt{2\pi r}\,\tilde{\sigma}_{21}(r,\theta)|_{\theta=0}\right\}\\ L_I &:= \lim_{r\to 0}\left\{\sqrt{2\pi r}\,\tilde{\mu}_{23}(r,\theta)|_{\theta=0}\right\}, \quad l_{II} := \lim_{r\to 0}\left\{\tilde{\mu}_{13}(r,\theta)|_{\theta=0}\right\}\end{aligned} \tag{9}$$

where subscripts I and II are referring to Mode I (crack opening) and Mode II (crack shearing) loading conditions, respectively. In a similar manner, the displacement and micro-rotation can be reported as:

$$\begin{Bmatrix} \tilde{u}_1 \\ \tilde{u}_2 \end{Bmatrix} = \frac{K_I}{2\mu}\sqrt{\frac{r}{2\pi}} \begin{Bmatrix} ((3-2\nu-\mathrm{Cos}\theta)S-2\nu)\mathrm{Cos}\dfrac{\theta}{2} \\ ((1-2\nu-\mathrm{Cos}\theta)S+2(1-\nu))\mathrm{Sin}\dfrac{\theta}{2} \end{Bmatrix} + \frac{K_{II}}{2\mu}\sqrt{\frac{r}{2\pi}} \begin{Bmatrix} ((3-2\nu+\mathrm{Cos}\theta)S+2(1-\nu))\mathrm{Sin}\dfrac{\theta}{2} \\ ((2\nu-1-\mathrm{Cos}\theta)S+2\nu)\mathrm{Cos}\dfrac{\theta}{2} \end{Bmatrix} + \dots \tag{10}$$

$$\tilde{\phi}_3 = \frac{L_I}{\gamma}\sqrt{\frac{2r}{\pi}}\mathrm{Sin}\frac{\theta}{2} + \frac{l_{II}}{\gamma} r\mathrm{Cos}\theta + \dots$$

2.2.2. The concept of J and I integrals

J-integral is a path independent line integral, proposed independently by Cherepanov (1967), and Rice (1968), that equals to the strain energy release rate, G, for linear elastic materials. For a crack with flat surfaces parallel to the $\tilde{x}_1$-axis, the *J-integral* of a micropolar medium takes the following form considering 2D case (Mühlhaus & Pasternak, 2002; Lubarda & Markenscoff, 2003):

$$J = \int_{\Gamma} \left(\frac{1}{2}(\tilde{\sigma}_{mn}\tilde{\varepsilon}_{mn} + \tilde{\mu}_{m3}\tilde{\chi}_{m3})\delta_{i1} - \tilde{\sigma}_{ij}\tilde{u}_{j,\bar{1}} - \tilde{\mu}_{i3}\tilde{\phi}_{3,\bar{1}} \right) n_i \mathrm{d}s, \quad i = 1,2 \tag{11}$$

where Γ is singularity free path surrounding the crack tip with a unit normal vector n_i. The integration is performed in counter-clockwise direction starting from any arbitrary point on lower crack face and ending at the upper one. Since *J-integral* is path independent, any singularity-free contour can be used for calculations. Here, for simplicity, the integration operations are performed on a vanishingly thin rectangle having a length of $2b$ and height of $2a$ such that $a << b$ and $a \to 0$. This allows the integrals over vertical lines to be ignored (Sun & Jin, 2011), and leads to following expression regarding the symmetric and antisymmetric boundary conditions for Mode I and Mode II:

$$J = 2\lim_{b\to 0}\int_{+b}^{-b} \left(\tilde{\sigma}_{21}\tilde{u}_{1,\bar{1}} + \tilde{\sigma}_{22}\tilde{u}_{2,\bar{1}} + \tilde{\mu}_{23}\tilde{\phi}_{3,\bar{1}} \right) \mathrm{d}\tilde{x}_1 \Big|_{\tilde{x}_2 = b^+} \tag{12}$$

Substituting the corresponding expressions of stress, couple stress, displacement and rotation fields, Eqs. (7), (8) and (10), into Eq. (12) with exploiting the chain rule gives;

$$J = \frac{(1+S)(1-\nu)}{4\mu}\left(K_I^2 + K_{II}^2\right) + \frac{L_I^2}{2\gamma} \tag{13}$$

It should be noted that, this is the exact expression reported in Yu et al. (2014) (see Eq. (32)) as well as Atkinson & Leppington (1977) (see Eq. (3.42)). As the main aim is to extract the value of SIFs and CSIF, one needs to calculate the integral in Eq. (11) along any singularity free contour near the crack tip, and equate it to Eq. (13). However, in order to distinguish the contribution of each SIFs and CSIF under mixed mode case, the concept of two state integral must be utilized (Chen & Shield, 1977; Stern et al., 1976). Accordingly,

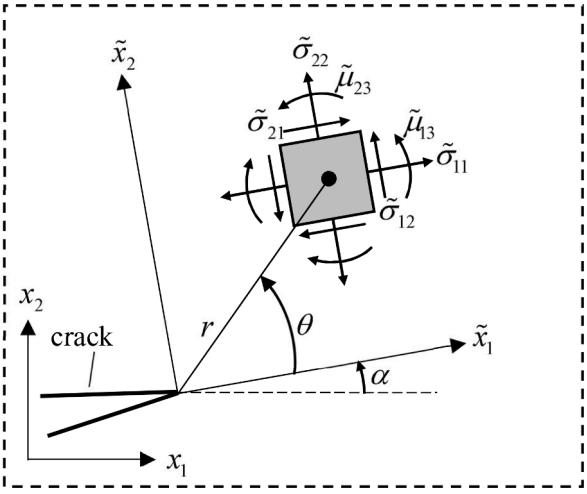

Fig. 1. Infinitesimal stress/couple-stress element at the crack tip.

by superimposing an admissible auxiliary field, denoted by superscript (a), on the actual/real state, a new form of *J-integral* is obtained:

$$J^{(a+r)} = \int_{\Gamma} \left(\begin{array}{c} \frac{1}{2}\left(\left(\widetilde{\sigma}^{a}_{mn} + \widetilde{\sigma}_{mn}\right)\left(\widetilde{\varepsilon}^{a}_{mn} + \widetilde{\varepsilon}_{mn}\right) + \left(\widetilde{\mu}^{a}_{m3} + \widetilde{\mu}_{m3}\right)\left(\widetilde{\chi}^{a}_{m3} + \widetilde{\chi}_{m3}\right)\right)\delta_{i1} \\ -\left(\widetilde{\sigma}^{a}_{ij} + \widetilde{\sigma}_{ij}\right)\left(\widetilde{u}^{a}_{j,\bar{1}} + \widetilde{u}_{j,\bar{1}}\right) - \left(\widetilde{\mu}^{a}_{i3} + \widetilde{\mu}_{i3}\right)\left(\widetilde{\phi}^{a}_{3,\bar{1}} + \widetilde{\phi}_{3,\bar{1}}\right) \end{array} \right) n_i ds$$

$$J^{(a+r)} = \frac{(1+S)(1-\nu)}{4\mu}\left(\left(K^{a}_{I} + K_{I}\right)^2 + \left(K^{a}_{II} + K_{II}\right)\right) + \frac{\left(L^{a}_{I} + L_{I}\right)^2}{2\gamma} \tag{14}$$

where the displacement, $\widetilde{u}^{a}_{i}$, rotation, $\widetilde{\phi}^{a}_{3}$, stress, $\widetilde{\sigma}^{a}_{ij}$, and couple-stress, $\widetilde{\mu}^{a}_{i3}$, fields are expressed in terms of auxiliary SIFs, K^{a}_{I}, K^{a}_{II}, and CSIF, L^{a}_{I}, by replacing those with the actual ones in Eqs. (7), (8) and (10) (Yau et al., 1980). The fact that the equilibrium equations and traction free boundary conditions should be satisfied for each individual case separately;

$$\text{Case1} : K^{a}_{I} = 1, K^{a}_{II} = L^{a}_{I} = 0, \quad \text{Case2} : K^{a}_{II} = 1, K^{a}_{I} = L^{a}_{I} = 0, \quad \text{Case3} : L^{a}_{I} = 1, K^{a}_{I} = K^{a}_{II} = 0 \tag{15}$$

allowing us to manipulate the kinematic relations as follows:

$$\widetilde{\varepsilon}^{a}_{ij} = \widetilde{u}^{a}_{j,\bar{i}}, \;\; \widetilde{\chi}^{a}_{j3} = \widetilde{\phi}^{a}_{3,\bar{j}} \tag{16}$$

which leads following equilibrium equations:

$$\widetilde{\sigma}^{a}_{ji,\bar{j}} = 0, \;\; \widetilde{\mu}^{a}_{j3,\bar{j}} = 0 \tag{17}$$

Accordingly, Eq. (14) results in

$$J^{(a+r)} = J^{(a)} + J^{(r)} + I^{(a,r)} \tag{18}$$

Here $J^{(a)}$ and $J^{(r)}$ stand for *J-integrals* that consist of terms related only to *auxiliary* and *real* fields, respectively, whereas $I^{(a,r)}$ is formed by the contribution of both and called as interaction (*I-integral*) integral:

$$I^{(a,r)} = \int P^{(a,r)}_{i1} n_i d\Gamma = \frac{1+S}{\dfrac{E}{1-\nu^2}}\left(K_I K^{a}_{I} + K_{II} K^{a}_{II}\right) + \frac{L_I L^{a}_{I}}{\gamma} \tag{19}$$

with

$$P^{(a,r)}_{i1} = \left(\widetilde{\sigma}^{a}_{mn}\widetilde{\varepsilon}_{mn} + \widetilde{\mu}^{a}_{m3}\widetilde{\chi}_{m3}\right)\delta_{i1} - \widetilde{\sigma}^{a}_{ij}\widetilde{u}_{j,\bar{1}} - \widetilde{\sigma}_{ij}\widetilde{u}^{a}_{j,\bar{1}} - \widetilde{\mu}^{a}_{i3}\widetilde{\phi}_{3,\bar{1}} - \widetilde{\mu}_{i3}\widetilde{\phi}^{a}_{3,\bar{1}} \tag{20}$$

Utilizing the equality in Eq. (19), SIFs and CSIF can be decoupled easily for each mode with the aid of interaction integral, $I^{(a,r)}$, also evident from Yu et al. (2014) (see Eqs. (35) and (36)):

$$K_I = \frac{I^{(a,r)}_{\text{Case1}} E}{(1-\nu^2)(1+S)}, \quad K_{II} = \frac{I^{(a,r)}_{\text{Case2}} E}{(1-\nu^2)(1+S)}, \quad L_I = I^{(a,r)}_{\text{Case3}}\gamma \tag{21}$$

As contour (line) is not optimal for calculation of $I^{(a,r)}$, it is more convenient to use the equivalent domain form of the integral that minimizes the local errors of contour integral (Qian et al., 2016; Yu & Kuna, 2021):

$$I^{(a,r)} = \int_{\Gamma} P^{(a,r)}_{i1} n_i d\Gamma = -\int_{A}\left(P^{(a,r)}_{i1,\bar{i}} q + P^{(a,r)}_{i1} q_{,\bar{i}}\right) d\widetilde{x}_1 d\widetilde{x}_2 \tag{22}$$

where q is the weight function. Following the detailed derivations presented in Appendix A, the final version of $I^{(a,r)}$ takes the form of;

$$I^{(a,r)} = \int_{A} \left\{ \begin{array}{l} \varepsilon_{ij3}\left(\widetilde{\sigma}^{a}_{ij}\widetilde{\phi}_{3,\bar{1}} - \widetilde{\sigma}_{ij}\widetilde{\phi}^{a}_{3,\bar{1}}\right) q + \\ \left(\widetilde{\sigma}^{a}_{ij}\widetilde{u}_{j,\bar{1}} + \widetilde{\sigma}_{ij}\widetilde{u}^{a}_{j,\bar{1}} + \widetilde{\mu}^{a}_{i3}\widetilde{\phi}_{3,\bar{1}} + \widetilde{\mu}_{i3}\widetilde{\phi}^{a}_{3,\bar{1}} - \left(\widetilde{\sigma}^{a}_{mn}\widetilde{\varepsilon}_{mn} + \widetilde{\mu}^{a}_{m3}\widetilde{\chi}_{m3}\right)\delta_{i1}\right) q_{,\bar{i}} \end{array} \right\} d\widetilde{x}_1 d\widetilde{x}_2 \tag{23}$$

2.3. Micropolar/XFEM model

Extended finite element method (XFEM) is developed by Belytschko & Black (1999); Daux et al. (2000); Dolbow (1999); Moes et al., (1999) as an extension of partition of unity approach (Melenk & Babuska, 1996) to model the discontinuities without the need to have conforming mesh with crack geometry and/or material interface (Huang et al., 2003; Sukumar & Prevost, 2003). This is achieved by locally enriching the nodes located in the influence domain of discontinuity and/or singularity through adding special functions in the standard FE approximation field(s). For a homogeneous isotropic micropolar medium with a pre-existing crack, as illustrated in Fig. 2, the nodes of element(s), that entirely split by crack and containing crack tip(s), are endowed with Heaviside and crack-tip related degrees of freedom (DOFs), respectively, considering both translational and rotational fields, denoted by superscripts, u and ϕ.

Heaviside step function, $H^u(\mathbf{x}), H^\phi(\mathbf{x})$, is used in modeling the strong discontinuity across the element that is caused by the crack split (Moes et al., 1999), and defined by the signed distance function, $\psi(\mathbf{x})$:

$$H^u(\mathbf{x}) = H^\phi(\mathbf{x}) = \left\{ \begin{matrix} +1 & \text{if} \psi(\mathbf{x}) > 0 \\ -1 & \text{if} \psi(\mathbf{x}) < 0 \end{matrix} \right\}, \quad \psi(\mathbf{x}) = \| \mathbf{x} - \mathbf{x}^* \| sign(\mathbf{n}.(\mathbf{x} - \mathbf{x}^*)) \tag{24}$$

where $\mathbf{x}$ is the global Cartesian coordinate of the point under investigation $\{x_1, x_2\}$ (node or Gauss sampling point) and $\mathbf{x}^*$ is the coordinate of closest point to $\mathbf{x}$ that lies on the crack face with a unit normal vector $\mathbf{n}$ (see Fig. 3). Accordingly, for points above and below the crack, Heaviside function takes the values of +1 and -1, respectively with having a discontinuity at the interface, via which the crack partition is successfully simulated. Meanwhile, crack tip enrichment functions, $\mathbf{\Phi}^u(\mathbf{r}), \mathbf{\Phi}^\phi(\mathbf{r})$, are used to model the singularity around the crack tip in an efficient manner by mimicking the asymptotic behavior of displacement and rotation fields with $\mathbf{r}$ referring to the local polar coordinates of the point $\{r, \theta\}$(see Fig. 3). This is achieved with the aid of radial and angular basis functions extracted from the analytical solutions of micropolar/LEFM problem under 2D case. For displacement field, same branch functions used in the classical case are employed (Fleming et al., 1997), while for rotation field, the singularity is covered by the first tip enrichment function following Eqs. (7) and (10) (Kapiturova et al., 2016):

$$\begin{aligned} \mathbf{\Phi}^u(\mathbf{r}) &= \{\Phi^1, \Phi^2, \Phi^3, \Phi^4\} = \left\{ \sqrt{r}\,\text{Sin}\frac{\theta}{2},\ \sqrt{r}\,\text{Cos}\frac{\theta}{2},\ \sqrt{r}\,\text{Sin}\frac{\theta}{2}\text{Sin}\theta,\ \sqrt{r}\,\text{Cos}\frac{\theta}{2}\text{Sin}\theta \right\} \\ \mathbf{\Phi}^\phi(\mathbf{r}) &= \{\Phi^1\} = \left\{ \sqrt{r}\,\text{Sin}\frac{\theta}{2} \right\} \end{aligned} \tag{25}$$

As the current form of Heaviside step and crack-tip functions violate the Kronecker-δ property, the corresponding formulation is modified through the shifting functions; $\overline{H}(\mathbf{x}_i), \overline{\Phi}(\mathbf{r}_i)$:

$$H(\mathbf{x}) - \overline{H}(\mathbf{x}_i) \quad \mathbf{\Phi}(\mathbf{r}) - \overline{\Phi}(\mathbf{r}_i), \quad i = 1, \ldots, 4 \tag{26}$$

At this point, the formation of the lists including the node sets for enrichment should be explained:

(i) First, the nodes of the element(s) that contains the crack tip(s) are enriched by crack-tip related DOFs. This is known as topological type enrichment in which the size of branch function enriched area varies depending on the discretization. For such a case, although the convergence rate can be further improved via adopting the fixed enrichment area scheme (geometrical enrichment) (Laborde et al., 2005 and Béchet et al., 2005), it is not considered in the present study following the fact that increasing the number of enriched nodes has an adverse influence on the conditioning properties of the resulting linear system, which seeks remedies (e.g. special blending strategies, higher order shape functions, preconditioning) to guarantee better convergence rates and higher accuracy (Belytschko et al., 2009; Deng et al., 2023; Fries 2008; Fries & Belytschko 2010; Gracie et al., 2008; Gupta et al., 2013; Tarancon et al., 2009; Tian & Wen 2015; Wen et al., 2023). Accordingly, no special blending treatment is considered herein as the error that is caused by the parasitic terms in the presence of partially crack-tip enriched elements are negligible in topological enrichment owing to their fewness in number, compared to geometrical one. Moreover, the existence of partially Heaviside enriched elements does not lead to any alterations in the approximation field due to shifting operation.

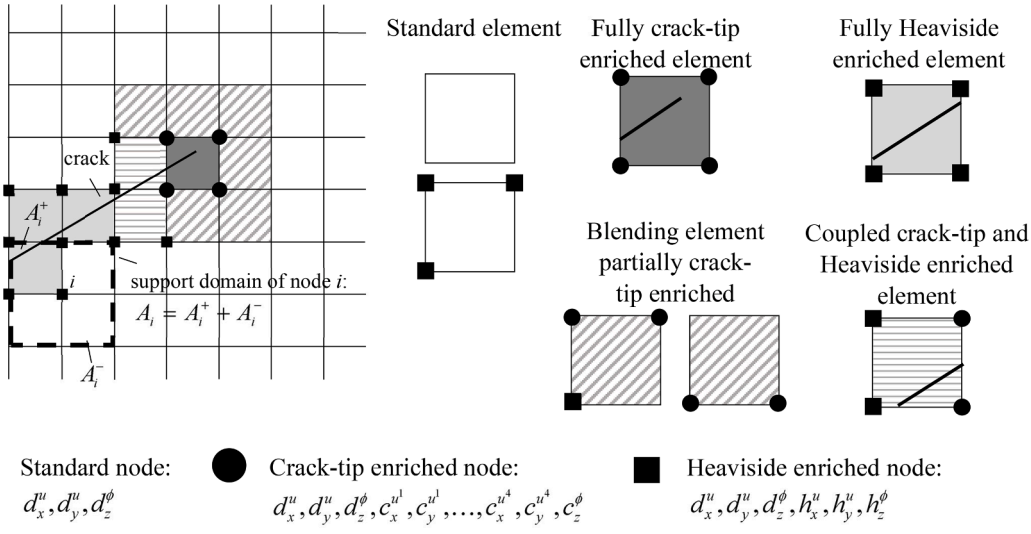

Fig. 2. The element and node types in extended finite element method (XFEM).

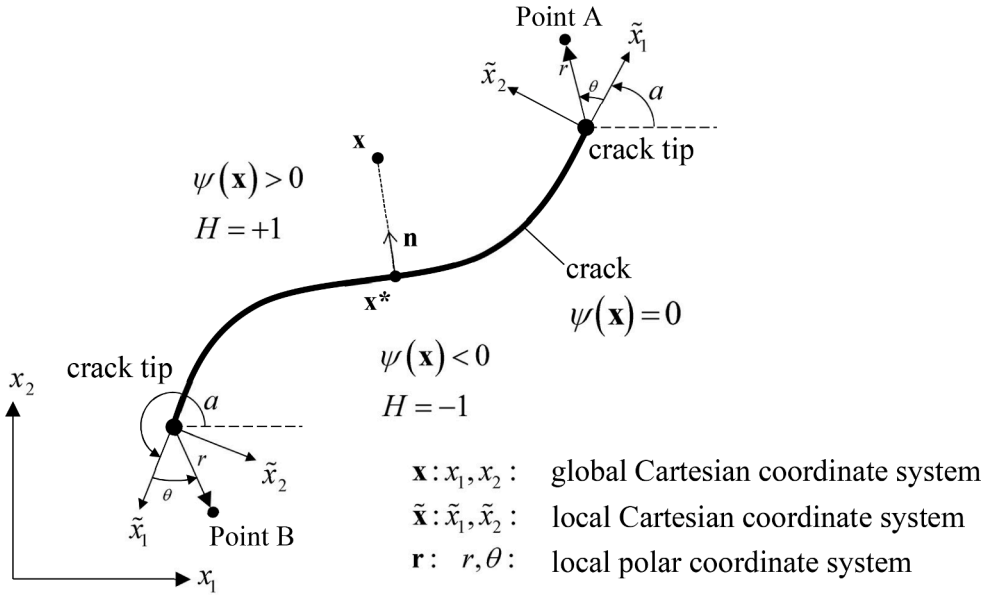

Fig. 3. The signed distance function and coordinate systems.

(ii) Secondly, the nodes of element(s) that is intersected by the crack is enriched with the step function while following exceptions must be kept in mind. For instance, the node(s) that belong to the element(s) containing the crack-tip(s) must be excluded as the discontinuity has already been accounted for through the first branch function. Moreover, one needs to pay attention to the ratio between partitioned areas, A_i^-, A_i^+, and support domain, $A_i = A_i^- + A_i^+$, of the Heaviside enriched node (See Fig. 2), as lower values result in ill-conditioned stiffness matrices (Daux et al., 2000; Moes et al., 1999).

Before any further progress, it should be noted that the solution of this problem is looked for in the standard Sobolev functional space for which the existence and uniqueness has already been pointed out (Chahine et al., 2006).

2.3.1. *Formulation of un-cracked (Standard) element*

Standard stiffness matrix is required for elements that do not contain any enriched node or for those partially enriched by Heaviside related DOFs but not split by the crack as illustrated in Fig. 2. The latter case can be justified through the fact that $H(\mathbf{x}) - \overline{H}(\mathbf{x}_i)$ equals to zero hence vanishes when the element is located above or below the crack. Accordingly, the nodal unknown vector of a standard first-order element m, $\mathbf{d}_m$, is represented in terms of nodal displacement and rotation vectors, $\mathbf{d}_m^u$,$\mathbf{d}_m^\phi$, containing standard translational; d_x^u, d_y^u, and rotational; d_z^ϕ, DOFs per each node (Fig. 4(a)):

$$\mathbf{d}_m = \begin{Bmatrix} \mathbf{d}_m^u \\ \mathbf{d}_m^\phi \end{Bmatrix} = \begin{Bmatrix} d_{x_1}^u & d_{y_1}^u & \dots & d_{y_4}^u & d_{z_1}^\phi & \dots & d_{z_4}^\phi \end{Bmatrix}_m^{\mathrm{T}} \tag{27}$$

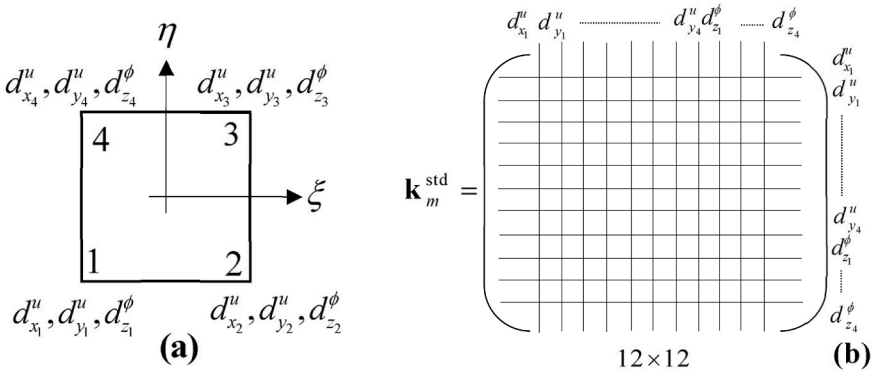

Fig. 4. (a) Standard element, (b) Formation of corresponding element stiffness matrix.

where subscripts refer to the node number, and T denotes transpose operator. The corresponding displacement and rotation fields $\mathbf{u}_m$, $\boldsymbol{\phi}_m$ are calculated with the aid of shape function matrices; $\mathbf{N}^{u-\mathrm{std}}$, and $\mathbf{N}^{\phi-\mathrm{std}}$:

$$\begin{aligned}
&\mathbf{u}_m = \begin{Bmatrix} u_1 \\ u_2 \end{Bmatrix}_m = \mathbf{N}(\boldsymbol{\xi})^{u-std}\,\mathbf{d}_m^u, \qquad \boldsymbol{\phi}_m = \{\phi_3\}_m = \mathbf{N}(\boldsymbol{\xi})^{\phi-std}\mathbf{d}_m^{\phi} \\
&\mathbf{N}(\boldsymbol{\xi})^{u-std} = \begin{bmatrix} N_1(\boldsymbol{\xi}) & 0 & \cdots & N_4(\boldsymbol{\xi}) & 0 \\ 0 & N_1(\boldsymbol{\xi}) & & 0 & N_4(\boldsymbol{\xi}) \end{bmatrix}_{2\times 8}, \mathbf{N}(\boldsymbol{\xi})^{\phi-std} = \begin{bmatrix} N_1(\boldsymbol{\xi}) & \cdots & N_4(\boldsymbol{\xi}) \end{bmatrix}_{1\times 4}
\end{aligned} \tag{28}$$

having components represented in terms of natural coordinate system, $\boldsymbol{\xi} = \{\xi,\eta\} \in [-1, +1]$:

$$N_1 = \frac{(1-\xi)(1-\eta)}{4}, \quad N_2 = \frac{(1+\xi)(1-\eta)}{4}, \quad N_3 = \frac{(1+\xi)(1+\eta)}{4}, \quad N_4 = \frac{(1-\xi)(1+\eta)}{4} \tag{29}$$

To obtain the corresponding strain and curvature fields of the element m; $\boldsymbol{\varepsilon}_m^{\mathrm{std}}$, $\boldsymbol{\chi}_m^{\mathrm{std}}$ the usual FE procedure is followed:

$$\boldsymbol{\varepsilon}_m^{\mathrm{std}} = \begin{bmatrix} \mathbf{L}_m\mathbf{N}^{u-\mathrm{std}} & \mathbf{M}\mathbf{N}^{\phi-\mathrm{std}} \end{bmatrix}\mathbf{d}_m = \mathbf{B}_m^{\varepsilon-\mathrm{std}}\mathbf{d}_m, \quad \boldsymbol{\chi}_m^{\mathrm{std}} = \begin{bmatrix} \mathbf{0} & \nabla_m\mathbf{N}^{\phi-\mathrm{std}} \end{bmatrix}\mathbf{d}_m = \mathbf{B}_m^{\chi-\mathrm{std}}\mathbf{d}_m \tag{30}$$

where differential operator matrix, $\mathbf{L}_m$, permutation vector, $\mathbf{M}$, and gradient operator vector, ∇_m, takes the following form with the aid of well-known inverse Jacobian matrix, $\mathbf{J}_m^{\mathrm{GN}}$:

$$\begin{aligned}
\mathbf{L}_m &= \begin{bmatrix} \frac{\partial}{\partial x_1} & 0 \\ 0 & \frac{\partial}{\partial x_2} \\ 0 & \frac{\partial}{\partial x_1} \\ \frac{\partial}{\partial x_2} & 0 \end{bmatrix} = \begin{bmatrix} \frac{\partial}{\partial \xi}J_{11}^{\mathrm{GN}} + \frac{\partial}{\partial \eta}J_{21}^{\mathrm{GN}} & 0 \\ 0 & \frac{\partial}{\partial \xi}J_{12}^{\mathrm{GN}} + \frac{\partial}{\partial \eta}J_{22}^{\mathrm{GN}} \\ 0 & \frac{\partial}{\partial \xi}J_{11}^{\mathrm{GN}} + \frac{\partial}{\partial \eta}J_{21}^{\mathrm{GN}} \\ \frac{\partial}{\partial \xi}J_{12}^{\mathrm{GN}} + \frac{\partial}{\partial \eta}J_{22}^{\mathrm{GN}} & 0 \end{bmatrix}_m, \quad \mathbf{M} = \begin{bmatrix} 0 \\ 0 \\ -1 \\ +1 \end{bmatrix} \\
\nabla_m &= \begin{bmatrix} \frac{\partial}{\partial x_1} \\ \frac{\partial}{\partial x_2} \end{bmatrix} = \begin{bmatrix} \frac{\partial}{\partial \xi}J_{11}^{\mathrm{GN}} + \frac{\partial}{\partial \eta}J_{21}^{\mathrm{GN}} \\ \frac{\partial}{\partial \xi}J_{12}^{\mathrm{GN}} + \frac{\partial}{\partial \eta}J_{22}^{\mathrm{GN}} \end{bmatrix}_m
\end{aligned} \tag{31}$$

where, $\mathbf{J}_m^{\mathrm{GN}} = \mathbf{J}_m^{\mathrm{NG}^{-1}}$, with $\mathbf{J}_m^{\mathrm{NG}}$ giving the direct mapping between global (G) and natural (N) coordinates. Eventually, for such a case, the element formulation is represented in terms of standard load, standard nodal unknown vectors, $\mathbf{f}_m^{\mathrm{std}}$, $\mathbf{d}_m$, and standard stiffness matrix, $\mathbf{k}_m^{\mathrm{std}}$(Fig. 4):

$$\mathbf{f}_m^{\mathrm{std}} = \mathbf{k}_m^{\mathrm{std}}\mathbf{d}_m \tag{32}$$

with

$$\mathbf{k}_m^{\mathrm{std}} = h\int_{-1}^{+1}\int_{-1}^{+1}\left(\mathbf{B}_m^{\varepsilon-\mathrm{std}^{\mathrm{T}}}\mathbf{D}^{\varepsilon}\mathbf{B}_m^{\varepsilon-\mathrm{std}} + \mathbf{B}_m^{\chi-\mathrm{std}^{\mathrm{T}}}\mathbf{D}^{\chi}\mathbf{B}_m^{\chi-\mathrm{std}}\right)|\mathbf{J}_m^{\mathrm{NG}}|\mathrm{d}\xi\mathrm{d}\eta \tag{33}$$

where h is the thickness of the element, and $|\mathbf{J}_m^{\mathrm{NG}}|$ is the determinant of the Jacobian matrix.

2.3.2. Formulation of cracked (Enriched) element

Heaviside step function enriched part of stiffness matrix, $\mathbf{k}_m^{\mathrm{hvs}}$, is required for element(s) that are completely split by the crack (see Fig. 2), while crack-tip enriched part of stiffness matrix, $\mathbf{k}_m^{\mathrm{ctp}}$, is derived for element(s) having at least one crack-tip enriched node. In such cases, following nodal unknown vectors, $\mathbf{h}_m$, $\mathbf{c}_m$, are emerged in addition to the standard one $\mathbf{d}_m$:

$$\begin{aligned}
\mathbf{h}_m &= \begin{Bmatrix} \mathbf{h}_m^u \\ \mathbf{h}_m^{\phi} \end{Bmatrix} = \begin{Bmatrix} h_{x_1}^u & h_{y_1}^u & \cdots & h_{y_4}^u & h_{z_1}^{\phi} & \cdots & h_{z_4}^{\phi} \end{Bmatrix}_m^{\mathrm{T}} \\
\mathbf{c}_m &= \begin{Bmatrix} \mathbf{c}_m^u \\ \mathbf{c}_m^{\phi} \end{Bmatrix} = \begin{Bmatrix} c_{x_1}^{u^1} & c_{y_1}^{u^1} & \cdots & c_{y_1}^{u^4} & \cdots & c_{x_4}^{u^1} & c_{y_4}^{u^1} & \cdots & c_{y_4}^{u4} & c_{z_1}^{\phi^1} & \cdots & c_{z_4}^{\phi^1} \end{Bmatrix}_m^{\mathrm{T}}
\end{aligned} \tag{34}$$

In the most general case, with all nodes endowed, the former has the same dimensions as the standard nodal unknown vector; 12×1, while the latter is a 36×1 vector regarding four functions per each translational DOF (4×2) and 1 function per rotational DOF (1×1), indicated by superscripts u^1, u^2, u^3, u^4 and ϕ^1, respectively. As in the usual case without *fixed enrichment area* approach, a node can be endowed with either Heaviside or crack-tip related DOFs as can be seen from Fig. 2, it is more convenient to represent the related shape functions as follows:

$$\mathbf{N}(\boldsymbol{\xi})_m^{u-hvs} = \begin{bmatrix} N_I(\boldsymbol{\xi})(H(\mathbf{x}) - \overline{H}(\mathbf{x}_1)) & 0 & \cdots \\ 0 & N_I(\boldsymbol{\xi})(H(\mathbf{x}) - \overline{H}(\mathbf{x}_1)) & \end{bmatrix}_{2\times 2H} \quad I \in \mathscr{N}_m^H$$
$$\mathbf{N}(\boldsymbol{\xi})_m^{\phi-hvs} = \begin{bmatrix} N_I(\boldsymbol{\xi})(H(\mathbf{x}) - \overline{H}(\mathbf{x}_1)) & \cdots \end{bmatrix}_{1\times H} \tag{35}$$

and

$$\mathbf{N}(\boldsymbol{\xi},\mathbf{r})_m^{u-ctp} = \begin{bmatrix} N_J(\boldsymbol{\xi})\left(\Phi^1(\mathbf{r}) - \ddot{\Phi}^1(\mathbf{r}_J)\right) & \cdots & 0 & \cdots \\ 0 & & N_J(\boldsymbol{\xi})\left(\Phi^4(\mathbf{r}) - \ddot{\Phi}^4(\mathbf{r}_J)\right) & \end{bmatrix}_{2\times 8C} \quad J \in \mathscr{N}_m^C$$
$$\mathbf{N}(\boldsymbol{\xi},\mathbf{r})_m^{\phi-ctp} = \begin{bmatrix} N_J(\boldsymbol{\xi})\left(\Phi^1(\mathbf{r}) - \ddot{\Phi}^1(\mathbf{r}_J)\right) \cdots \end{bmatrix}_{1\times C} \tag{36}$$

where $\mathscr{N}_m^H$ and $\mathscr{N}_m^C$ gives the lists of nodes in an element m that are associated with the Heaviside and crack-tip enrichments, respectively, while H, C are the number of nodes in those sets. Accordingly, the approximate displacement and micro-rotation fields are written as;

$$\begin{aligned} \mathbf{u}_m &= \mathbf{N}(\boldsymbol{\xi})^{u-\text{std}}\mathbf{d}_m^u + \mathbf{N}(\boldsymbol{\xi})_m^{u-\text{hvs}}\mathbf{h}_m^u + \mathbf{N}(\boldsymbol{\xi},\mathbf{r})_m^{u-\text{ctp}}\mathbf{c}_m^u \\ \boldsymbol{\phi}_m &= \mathbf{N}(\boldsymbol{\xi})^{\phi-\text{std}}\mathbf{d}_m^\phi + \mathbf{N}(\boldsymbol{\xi})_m^{\phi-\text{hvs}}\mathbf{h}_m^\phi + \mathbf{N}(\boldsymbol{\xi},\mathbf{r})_m^{\phi-\text{ctp}}\mathbf{c}_m^\phi \end{aligned} \tag{37}$$

for which the explicit expressions of second and third terms are

$$\begin{aligned} \mathbf{N}(\boldsymbol{\xi})_m^{u-hvs}\mathbf{h}_m^u &= \sum_{I\in\mathscr{N}_m^H} N_I(\boldsymbol{\xi})(H(\mathbf{x}) - \overline{H}(\mathbf{x}_I))\left\{ h_{x_I}^u \quad h_{y_I}^u \right\}_m^T \\ \mathbf{N}(\boldsymbol{\xi},\mathbf{r})_m^{u-ctp}\mathbf{c}_m^u &= \sum_{J\in\mathscr{N}_m^C}\sum_{f=1}^{4} N_J(\boldsymbol{\xi})\left(\Phi^f(\mathbf{r}) - \overline{\Phi}^f(\mathbf{r}_J)\right)\left\{ c_{x_J}^{u^f} \quad c_{y_J}^{u^f} \right\}_m^T \\ \mathbf{N}(\boldsymbol{\xi})_m^{\phi-hvs}\mathbf{h}_m^\phi &= \sum_{I\in\mathscr{N}_m^H} N_I(\boldsymbol{\xi})(H(\mathbf{x}) - \overline{H}(\mathbf{x}_I))\left\{ h_{z_I}^\phi \right\}_m \\ \mathbf{N}(\boldsymbol{\xi},\mathbf{r})_m^{\phi-ctp}\mathbf{c}_m^\phi &= \sum_{J\in\mathscr{N}_m^C} N_J(\boldsymbol{\xi})\left(\Phi^1(\mathbf{r}) - \overline{\Phi}^1(\mathbf{r}_J)\right)\left\{ c_{z_J}^{\phi^1} \right\}_m \end{aligned} \tag{38}$$

Here $\overline{H}(\mathbf{x}_I)$ is the value of Heaviside function at node I, which equals to either +1 or -1 depending on the signed distance function while $\overline{\Phi}^f(\mathbf{r}_J)$ is the value of corresponding branch function at node J. As the contribution of standard part has already been discussed in a detailed way in the previous section, we focus our attention to the latter ones, i.e. Heaviside and crack-tip enriched parts, leading to corresponding strain/curvature matrices:

$$\begin{aligned} \underbrace{\mathbf{B}_m^{\varepsilon-\text{hvs}}}_{4\times 3H} &= \left[\underbrace{\mathbf{L}_m}_{4\times 2}\underbrace{\mathbf{N}_m^{u-\text{hvs}}}_{2\times 2H} \quad \underbrace{\mathbf{M}}_{4\times 1}\underbrace{\mathbf{N}_m^{\phi-\text{hvs}}}_{1\times H} \right], \quad \underbrace{\mathbf{B}_m^{\chi-\text{std}}}_{2\times 3H} = \left[\underbrace{\mathbf{0}}_{2\times 2H} \quad \underbrace{\nabla_m}_{2\times 1}\underbrace{\mathbf{N}_m^{\phi-\text{hvs}}}_{1\times H} \right] \\ \underbrace{\mathbf{B}_m^{\varepsilon-\text{ctp}}}_{4\times 9C} &= \left[\underbrace{\mathbf{L}_m}_{4\times 2}\underbrace{\mathbf{N}_m^{u-\text{ctp}}}_{2\times 8C} \quad \underbrace{\mathbf{M}}_{4\times 1}\underbrace{\mathbf{N}_m^{\phi-\text{ctp}}}_{1\times C} \right], \quad \underbrace{\mathbf{B}_m^{\chi-\text{ctp}}}_{2\times 9C} = \left[\underbrace{\mathbf{0}}_{2\times 8C} \quad \underbrace{\nabla_m}_{2\times 1}\underbrace{\mathbf{N}_m^{\phi-\text{ctp}}}_{1\times C} \right] \end{aligned} \tag{39}$$

which includes the derivative of Heaviside and branch functions due to the differentiation operations in $\mathbf{L}$ and ∇;

$$\begin{aligned} &\frac{\partial N_I(\boldsymbol{\xi})}{\partial x_j}\left(H(\mathbf{x}) - \ddot{H}(\mathbf{x}_I)\right) + \frac{\partial H(\mathbf{x})}{\partial x_j}N_I(\boldsymbol{\xi}) \quad j = 1,2 \\ &\frac{\partial N_J(\boldsymbol{\xi})}{\partial x_j}\left(\Phi^f(\mathbf{r}) - \ddot{\Phi}^f(\mathbf{r}_J)\right) + \frac{\partial \Phi^f(\mathbf{r})}{\partial x_j}N_J(\boldsymbol{\xi}) \end{aligned} \tag{40}$$

Owing to the fact that the derivative of Heaviside function, Dirac delta; $\delta(\mathbf{x})$, is zero everywhere except for the interface, this part vanishes;

$$\frac{\partial H(\mathbf{x})}{\partial x_j} = \delta(\mathbf{x}) = \left\{ \begin{matrix} 0 & \text{if } \psi(\mathbf{x}) \neq 0 \\ \infty & \text{if } \psi(\mathbf{x}) = 0 \end{matrix} \right\} \tag{41}$$

while for the rest, chain rule must be employed. Here the derivative of interpolation function has already been given explicitly in Eq. (31), hence for branch functions;

$$\frac{\partial \Phi^f(\mathbf{r})}{\partial x_j} = \left(\frac{\partial \Phi^f(\mathbf{r})}{\partial r}J_{11}^{\text{LP}} + \frac{\partial \Phi^f(\mathbf{r})}{\partial \theta}J_{21}^{\text{LP}}\right)J_{1j}^{\text{GL}} + \left(\frac{\partial \Phi^f(\mathbf{r})}{\partial r}J_{12}^{\text{LP}} + \frac{\partial \Phi^f(\mathbf{r})}{\partial \theta}J_{22}^{\text{LP}}\right)J_{2j}^{\text{GL}} \tag{42}$$

where $\mathbf{J}^{\mathrm{LP}}$ and $\mathbf{J}^{\mathrm{GL}}$are the well-known matrices, used for transformation between global Cartesian (G) – local Cartesian (L) and local Cartesian (L) – local polar (P) coordinate systems, respectively:

$$\mathbf{J}^{\mathrm{GL}} = \begin{bmatrix} \cos\alpha & \sin\alpha \\ -\sin\alpha & \cos\alpha \end{bmatrix}, \quad \mathbf{J}^{\mathrm{LP}} = \begin{bmatrix} \cos\theta & -r\sin\theta \\ \sin\theta & r\cos\theta \end{bmatrix}^{-1} \tag{43}$$

where α refers to counter clock-wise angle from global horizontal to local horizontal axes. Consequently, for an element m, the formulation includes six sub-matrices in the most general case:

$$\begin{Bmatrix} \mathbf{f}_m^{\mathrm{std}} \\ \mathbf{f}_m^{\mathrm{hvs}} \\ \mathbf{f}_m^{\mathrm{ctp}} \end{Bmatrix} = \begin{bmatrix} \mathbf{k}_m^{\mathrm{std-std}} & \mathbf{k}_m^{\mathrm{std-hvs}} & \mathbf{k}_m^{\mathrm{std-ctp}} \\ \mathbf{k}_m^{\mathrm{hvs-std}} & \mathbf{k}_m^{\mathrm{hvs-hvs}} & \mathbf{k}_m^{\mathrm{hvs-ctp}} \\ \mathbf{k}_m^{\mathrm{std-hvs}} & \mathbf{k}_m^{\mathrm{ctp-hvs}} & \mathbf{k}_m^{\mathrm{ctp-ctp}} \end{bmatrix} \begin{Bmatrix} \mathbf{d}_m \\ \mathbf{h}_m \\ \mathbf{c}_m \end{Bmatrix} \tag{44}$$

with

$$\mathbf{k}_m^{\mathrm{a-b}} = h \int_{-1}^{+1} \int_{-1}^{+1} \left(\mathbf{B}_m^{\varepsilon-\mathrm{a}^{\mathrm{T}}} \mathbf{D}^{\varepsilon} \mathbf{B}_m^{\varepsilon-\mathrm{b}} + \mathbf{B}_m^{\gamma-\mathrm{a}^{\mathrm{T}}} \mathbf{D}^{\gamma} \mathbf{B}_m^{\gamma-\mathrm{b}} \right) \left| \mathbf{J}_m^{\mathrm{NG}} \right| \mathrm{d}\xi \mathrm{d}\eta, \qquad \mathrm{a,b} : \mathrm{std, hvs, ctp} \tag{45}$$

while it is clear that; $\mathbf{k}_m^{\mathrm{a-b}} = \mathbf{k}_m^{\mathrm{b-a}^{\mathrm{T}}}$. In Fig. 5, the construction of endowed stiffness matrices is given for a coupled crack-tip Heaviside enriched element.

2.3.3. Numerical integration

One of the main challenges in XFEM arises during calculation of stiffness matrices and equivalent domain form of *I-integral* due to discontinuous and singular nature of bases functions. In such cases, the integrands are no longer continuous polynomials, which leads

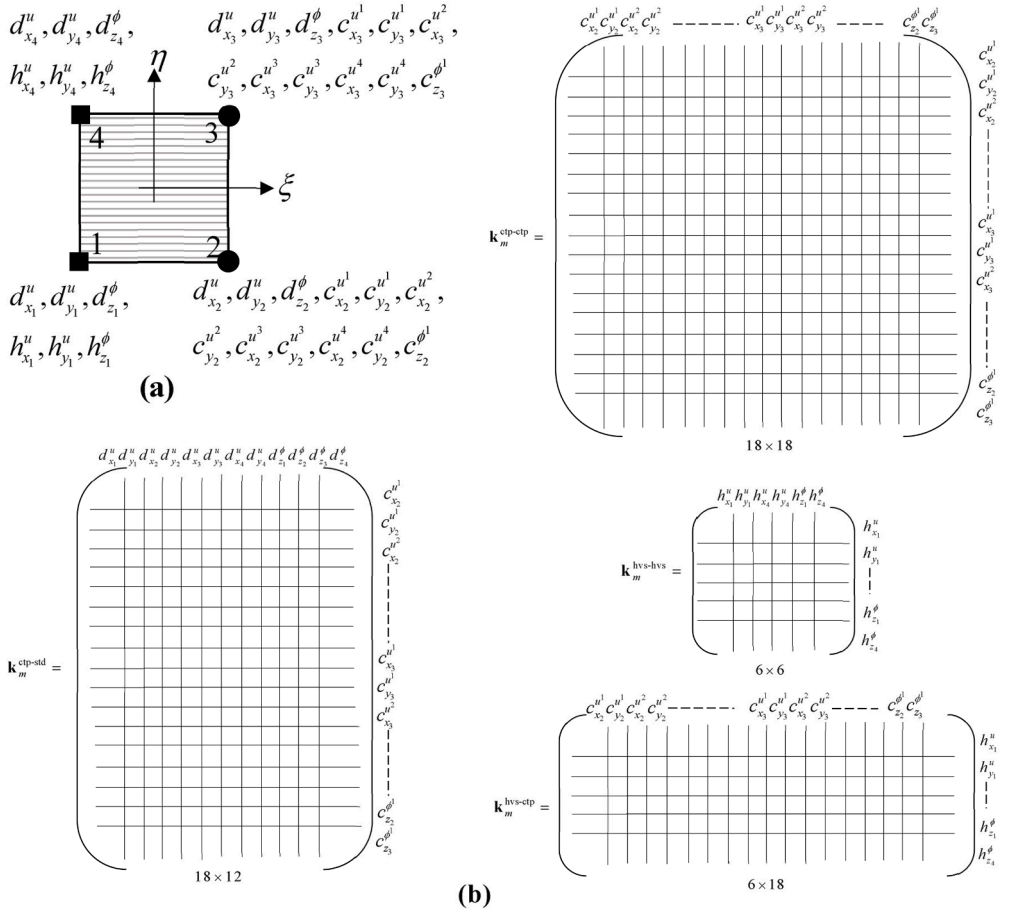

Fig. 5. (a) Coupled enriched element, (b) Formation of endowed element stiffness matrices.

to loss in accuracy when conventional Gauss quadrature approach is employed over the whole element. One can avoid this by dividing element into sub-quads or sub-triangles to handle numerical integrations separately as suggested by Dolbow 1999. Herein the former approach is conducted regarding its ease in implementation and efficiency in computation, whereas the latter one requires the use of computational geometry algorithms. Nevertheless, it should be realized that, the integrations performed on sub-quads containing the crack interface (highlighted by yellow in Fig. 6) will be inexact as it features a jump in approximate field, yet the accuracy can be increased by increasing the number of sub-quads. Accordingly, for an enriched element that is divided into $n_{\text{subx}} \times n_{\text{suby}}$ sub-quads, each denoted by q as illustrated in Fig. 6, one can calculate stiffness matrix as follows with considering 2 Gauss sampling point along each direction:

$$\begin{aligned}
\mathbf{k}_m^{a-b} &= \sum_{q=1}^{n_{subx}\times n_{suby}} \sum_{p=1}^{2}\sum_{r=1}^{2} \mathbf{K}_m^{a-b}\left(\xi_{qp},\eta_{qr}\right) w_{qp} w_{qr}, \qquad a,b : std, hvs, ctp \\
\mathbf{K}_m^{a-b}\left(\xi_{qp},\eta_{qr}\right) &= h\left(\mathbf{B}_m^{\varepsilon-a^T}\mathbf{D}^{\varepsilon}\mathbf{B}_m^{\varepsilon-b} + \mathbf{B}_m^{\chi-a^T}\mathbf{D}^{\chi}\mathbf{B}_m^{\chi-b}\right)\left|\mathbf{J}_m^{NG}\right|
\end{aligned} \tag{46}$$

with $\xi_{qp}, \eta_{qr}, w_{qp}, w_{qr}$ being the components of $\boldsymbol{\xi}_q, \boldsymbol{\eta}_q, \boldsymbol{w}_q$ vectors, that includes natural coordinates and weights of Gauss sampling points in the sub-quad q:

$$\begin{aligned}
\boldsymbol{\xi}_q &= \frac{\xi_{ql2}-\xi_{ql1}}{2}\begin{Bmatrix} +1/\sqrt{3} \\ -1/\sqrt{3} \end{Bmatrix} + \frac{\xi_{ql2}+\xi_{ql1}}{2}, \quad \boldsymbol{\eta}_q = \frac{\eta_{ql2}-\eta_{ql1}}{2}\begin{Bmatrix} +1/\sqrt{3} \\ -1/\sqrt{3} \end{Bmatrix} + \frac{\eta_{ql2}+\eta_{ql1}}{2} \\
\boldsymbol{w}_q &= \frac{\xi_{ql2}-\xi_{ql1}}{2}\,\frac{\eta_{ql2}-\eta_{ql1}}{2}\begin{Bmatrix} 1 \\ 1 \end{Bmatrix}
\end{aligned} \tag{47}$$

It should be noted that, as strain and curvature matrices of enriched elements might contain terms in cylindrical coordinates due to branch functions, necessary transformation between natural and local cylindrical coordinate systems should be performed when necessary.

2.3.4. Extraction of SIFs and CSIF

As previously mentioned, SIFs and CSIF are extracted using equivalent domain form of *I-integral*, which can be re-written as follows considering XFEM discretization and numerical integration scheme discussed above:

$$I^{(a,r)} = \sum_{s\in\mathcal{N}^I}\left(\sum_{q=1}^{n_{subx}\times n_{suby}}\sum_{p=1}^{2}\sum_{r=1}^{2} F_s\left(\xi_{qp},\eta_{qr}\right)\left|\mathbf{J}^{GL}\right|\left|\mathbf{J}_s^{NG}\right| w_{qp} w_{qr}\right) \tag{48}$$

Here $\mathcal{N}^I$ is a set including the elements residing and intersecting the circle centred at crack tip and having a radius r_I (Fig. 6) while F_s can be expressed as follows according to Eq. (23):

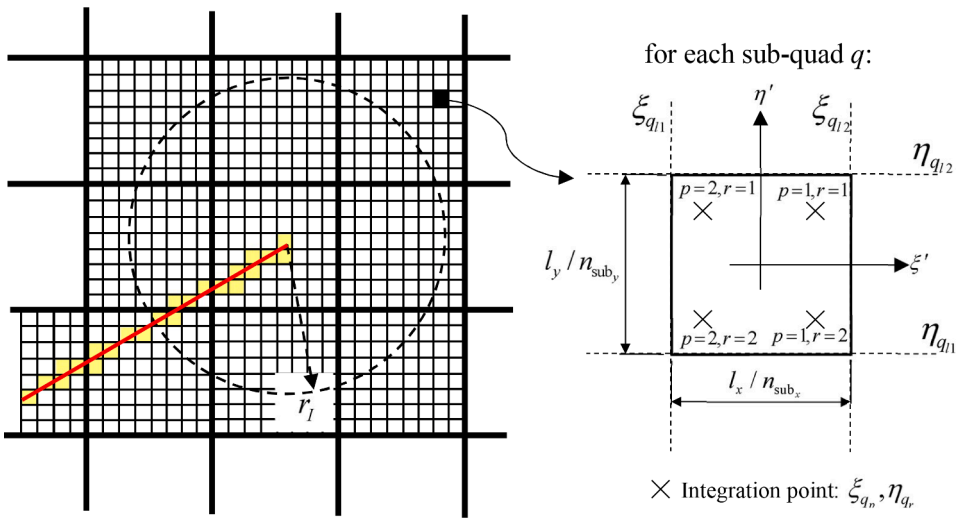

Fig. 6. Sub-quads used in integration of enriched linear elements and illustration of *I/J-integral* domain defined by radius r_I.

$$F_s = \left[\begin{array}{l} \left(\widetilde{\sigma}_{21}\widetilde{\phi}^a_{3,\bar{1}} - \widetilde{\sigma}_{12}\widetilde{\phi}^a_{3,\bar{1}} + \widetilde{\sigma}^a_{12}\widetilde{\phi}_{3,\bar{1}} - \widetilde{\sigma}^a_{21}\widetilde{\phi}_{3,\bar{1}} \right) q + \\ \left(-\overline{U} + \widetilde{\sigma}^a_{11}\widetilde{u}_{1,\bar{1}} + \widetilde{\sigma}^a_{12}\widetilde{u}_{2,\bar{1}} + \widetilde{\sigma}_{11}\widetilde{u}^a_{1,\bar{1}} + \widetilde{\sigma}_{12}\widetilde{u}^a_{2,\bar{1}} + \widetilde{\mu}^a_{13}\widetilde{\phi}_{3,\bar{1}} + \widetilde{\mu}_{13}\widetilde{\phi}^a_{3,\bar{1}} \right) q_{,\bar{1}} + \\ + \left(\widetilde{\sigma}^a_{21}\widetilde{u}_{1,\bar{1}} + \widetilde{\sigma}^a_{22}\widetilde{u}_{2,\bar{1}} + \widetilde{\sigma}_{21}\widetilde{u}^a_{1,\bar{1}} + \widetilde{\sigma}_{22}\widetilde{u}^a_{2,\bar{1}} + \widetilde{\mu}^a_{23}\widetilde{\phi}_{3,\bar{1}} + \widetilde{\mu}_{23}\widetilde{\phi}^a_{3,\bar{1}} \right) q_{,\bar{2}} \end{array} \right]_s \tag{49}$$

The weight function, q, defined as below, has a smooth nature such that it equals to unity and zero for points inside and outside of the circle, respectively.

$$q(\boldsymbol{\xi}) = \sum_{i=1}^{4} N_i(\boldsymbol{\xi}) q_i \qquad \begin{array}{l} q_i = 1 \quad \text{for nodes inside the circle} \\ q_i = 0 \quad \text{for odes outside the circle} \end{array} \tag{50}$$

It should be noted that, attention has to be paid for proper calculation of derivatives of weight function, and approximate displacement and rotation fields of both auxiliary and real states, following the fact that; $\widetilde{\mathbf{u}}_s = \mathbf{J}^{\mathrm{GL}}\mathbf{u}_s$, $\widetilde{\phi}_s = \phi_s$.

3. Numerical simulations

In this section, the results obtained from combined micropolar/XFEM model are compared with the ones available in the literature (Atroshchenko & Bordas, 2015; Diegele et al., 2004; Paul & Sridharan, 1981; Yu et al., 2014) to demonstrate the accuracy and versatility of the approach, and a case study is performed on an oblique edge crack specimen via focusing on the effect of non-locality.

3.1. Validation with literature case studies

The validation of the micropolar/XFEM model is attained through three benchmark problems for which the basic fracture parameters, obtained for Mode I and Mode II cases considering low, moderate and high non-localities, are commented on for various mesh configurations and *I/J-integral* radius. In all examples, the domain is uniformly discretized and the numerical integration procedure is performed by dividing enriched elements into 4 × 4 sub-quads, each with 2 × 2 Gauss sampling points.

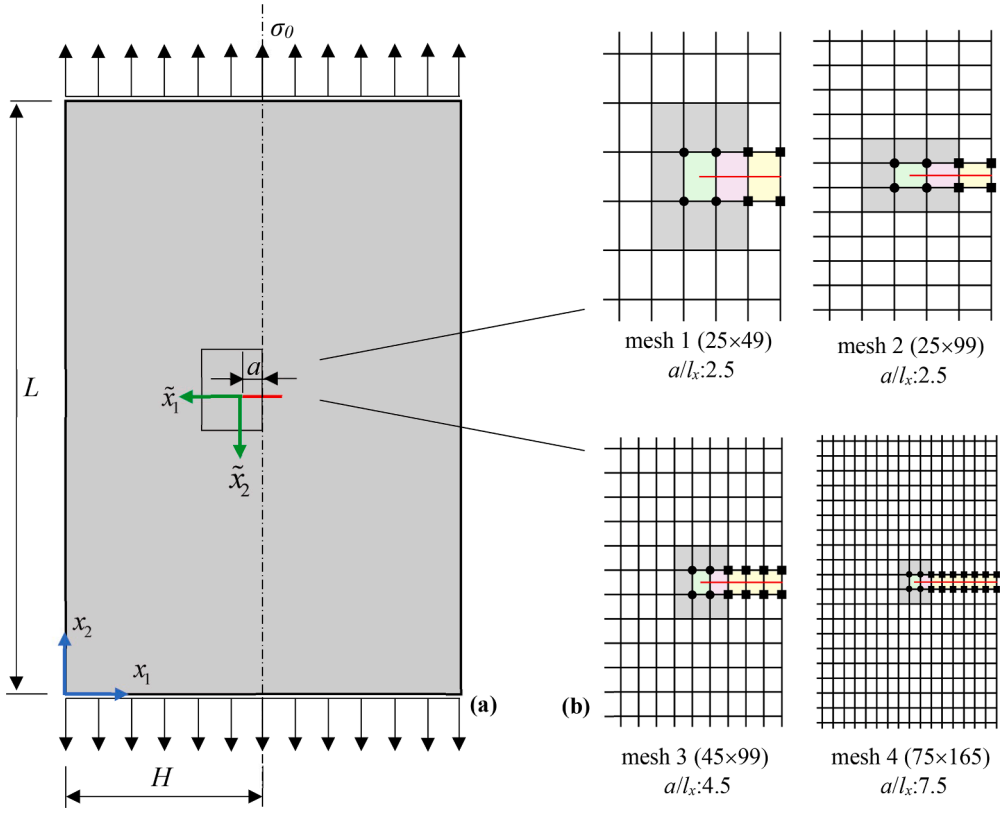

Fig. 7. (a) Schematic of the Griffith Problem considering whole model, and (b) corresponding discretization at the vicinity of the crack tip with l_x referring to element length.

3.1.1. Infinite plate with a central crack under tension (Griffith problem)

As the first validation test, SIF; K_I, CSIF; L_I, and crack opening displacement, $u_0 = u_2(H, L/2)$, of an infinite micropolar plate with a central crack under tension, leading to Mode I case (also known as Griffith Problem), is investigated. The dimensions of the XFEM model is arranged to mimic an almost infinite domain (Huang et al., 2003):

$$H = 10\,(\text{mm}), \quad L = 3H, \quad a = 0.1H \tag{51}$$

where the geometric quantities *H, L* and *a* refer to half width, vertical length and half crack size, respectively (Fig. 7(a)). With exploiting the symmetric nature of the problem, only one-half of the structure needs to be modeled via imposing necessary loading and boundary conditions:

$$\begin{aligned} &\sigma_{22}(x_1, L) = -\sigma_{22}(x_1, 0) = \sigma_0 = 100\,(\text{MPa}) \\ &u_1(H, x_2) = 0, \quad \phi_3(H, x_2) = 0 \end{aligned} \tag{52}$$

For all mesh configurations, the number of elements along both directions are selected to be odd to ensure that the crack tip lies inside the element, and crack surface cut through them (Fig. 7(b)). Here, the material properties are chosen in accordance with the literature (Atroshchenko & Bordas, 2015; Paul & Sridharan, 1981; Yu et al., 2014), indicating a relatively low level of micropolarity/non-locality:

$$E = 2100(MPa),\ \nu = 0.25,\ \begin{matrix} l_c = 0.353553(mm) \\ l_c/a = 0.353553 \end{matrix},\ N = 0.353553 \tag{53}$$

The results in the reference studies are listed in Table 1, after non-dimensionalization:

$$\overline{u}_0 = u_0 \frac{2\mu}{\sigma_0 a}, \quad \overline{K}_I = \frac{K_I}{\sigma_0\sqrt{\pi a}}, \quad \overline{L}_I = \frac{L_I}{\sigma_0 a\sqrt{\pi a}} \tag{54}$$

The literature (see Table 1) clearly shows the stiffening effect of micropolarity: the maximum opening between crack faces is decreased by 13 % compared to the classical case, $\overline{u}_0 = 1.5$(Tada et al., 2000); whereas K_I, seems to have an increasing trend for the considered parameter set since for local case, $\overline{K}_I^{\text{local}} = 1.0$ (Tada et al., 2000). As an interesting point, L_I, being negative can be explained through the inverse relation between positive direction of the couple stress component, μ_{23}, (see Fig. 2) and crack opening mechanism, such that the bond bending between material particles, located at the opposite sides of crack tip, promotes crack opening only if $\mu_{23} < 0$ (see Fig. 7 in Dyskin & Pasternak 2015), leading $L_I < 0$ (Eq. $(9)_3$).

After the interpretation of the results in literature, the effectiveness of the proposed model is investigated by reporting the fracture parameters obtained through developed micropolar/XFEM model in Table 2 considering four different mesh configurations, and various *I/J-integral* radii. The relative error is calculated as follows using the values in Paul & Sridharan 1981 as reference.

$$\%err = \left| \frac{(\overline{u}_0, \overline{K}_I, \overline{L}_I)|_{\text{XFEM}} - (\overline{u}_0, \overline{K}_I, \overline{L}_I)|_{\text{ref}}}{(\overline{u}_0, \overline{K}_I, \overline{L}_I)|_{\text{ref}}} \right| \times 100 \tag{55}$$

From Table 2, we can conclude that K_I becomes independent of the integral domain as r_I increases, such that $r_I \geq 1.75\, l_x$, $r_I \geq 2.25\, l_x$ and $r_I \geq 3.0\, l_x$ gave converged results for mesh 1–2, 3 and 4, respectively, with only 1.06 %, 0.24 %, 0.40 % and 0.27 % error, where l_x refers to element length along x_1-axis as an indicator of mesh refinement. The highest error for K_I, that is obtained for the smallest r_I radius ($r_I = 0.2a$ gave 3.13 % and 3.40 % error for mesh 3 and mesh 4, respectively) is attributed to the characteristics of the real stress field, $\widetilde{\sigma}$, (substituted into interaction integral) which tends to approach infinity as getting closer to the crack tip (Eq. (7)), and causing higher error rates.

For L_I, on the other hand, the errors have a more profound characteristic and a different trend. Although mesh refinement increases the accuracy for the converged values of L_I, such that $r_I = 0.9a$ resulted in 6.37 %, 6.17 %, 4.56 % and 2.85 % errors, respectively for meshes 1 to 4, smaller r_I yields better results. This higher dependency of L_I on the mesh configuration can be associated with the pronounced variation of micro-rotation field along the crack faces, which changes drastically compared to the displacement field (see Figs. 15 and 16 in Atroshchenko & Bordas, 2015), hence requires a finer discretization. Secondly, ρ; the size of the region dominated by the asymptotic part of micro-rotation field, is very small compared to internal characteristic length ($\rho << l_c$) (see Fig. 16 in Atroshchenko & Bordas, 2015), suggesting that auxiliary rotation field, $\widetilde{\phi}^a$, (substituted into interaction integral) is valid for small r_I.

At this point, it should be noted that, although the errors in Atroshchenko & Bordas, 2015 and Yu et al. 2014 (see Table 1) are lower than the ones reported herein, in the corresponding studies, the discretization at the crack tip and along the crack faces are substantially refined. For instance; in Yu et al. 2014, 12 singular elements are located at each crack tip as opposed to only 1 element

Table 1
Fracture parameters reported in literature for Griffith problem of Cauchy and micropolar plates.

	Reference	Method	$\overline{u}_0$	$\overline{K}_I$	$\overline{L}_I$
Cauchy	Tada et al., 2000	Analytical	1.5000	1.0000	–
Micropolar	Paul & Sridharan, 1981	Analytical expressions solved numerically	1.3022	1.0150	-0.0676
	Yu et al., 2014	Finite element model enriched for discontinuity with Heaviside-step function	–	1.0149	-0.0674
	Atroshchenko & Bordas, 2015	Standard boundary element method	1.3022	1.0222	-0.0676

Table 2
Non-dimensional fracture parameters obtained by the present micropolar/XFEM model for Griffith problem regarding various element size (l_x) and integral radius (r_I / a) with the relative errors calculated with respect to Paul & Sridharan, 1981.

	mesh 1 ($l_x = a/2.5$)	mesh 2 ($l_x = a/2.5$)	mesh 3 ($l_x = a/4.5$)	mesh 4 ($l_x = a/7.5$)
$\bar{u}_0$	1.2490 (4.09 %)	1.2676 (2.66 %)	1.2787 (1.80 %)	1.2910 (0.86 %)
$\bar{K}_I\,(r_I = 0.2a)$	–	–	1.0467 (3.13 %)	1.0495 (3.40 %)
$\bar{K}_I\,(r_I = 0.4a)$	1.0398 (2.44 %)	1.0411 (2.57 %)	1.0305 (1.53 %)	1.0178 (0.27 %)
$\bar{K}_I\,(r_I = 0.5a)$	1.0398 (2.44 %)	1.0279 (1.27 %)	1.0191 (0.40 %)	1.0184 (0.34 %)
$\bar{K}_I\,(r_I = 0.7a)$	1.0257 (1.06 %)	1.0126 (0.24 %)	1.0158 (0.08 %)	1.0184 (0.33 %)
$\bar{K}_I\,(r_I = 0.9a)$	1.0257 (1.06 %)	1.0146 (0.04 %)	1.0166 (0.15 %)	1.0185 (0.35 %)
$\bar{L}_I\,(r_I = 0.2a)$	–	–	-0.06544 (3.20 %)	-0.06693 (0.98 %)
$\bar{L}_I\,(r_I = 0.4a)$	-0.06315 (6.58 %)	-0.06409 (5.20 %)	-0.06496 (3.91 %)	-0.06547 (3.15 %)
$\bar{L}_I\,(r_I = 0.5a)$	-0.06315 (6.58 %)	-0.06359 (5.93 %)	-0.06421 (5.02 %)	-0.06559 (2.98 %)
$\bar{L}_I\,(r_I = 0.7a)$	-0.06330 (6.37 %)	-0.06322 (6.58 %)	-0.06436 (4.79 %)	-0.06559 (2.97 %)
$\bar{L}_I\,(r_I = 0.9a)$	-0.06330 (6.37 %)	-0.06343 (6.17 %)	-0.06452 (4.56 %)	-0.06567 (2.85 %)

considered herein. Similarly, in Atroshchenko & Bordas, 2015, each crack face contains 193 elements that are gradually refined towards the tip, whereas here along the crack geometry there exists 3 to 8 elements for different meshes.

In overall, it can be concluded that, for K_I, even a model with a coarse mesh and few elements along the crack (e.g. mesh 2) provides converged results with a very high accuracy (0.24 % error), whereas for L_I, one should pay attention to the right choice of integral radius, r_I. Nevertheless, the capability and versatility of the presented XFEM model for low level of non-locality under Mode I is highlighted.

3.1.2. *Finite plate with an edge crack under tension*

As the second validation test, the SIF and CSIF (K_I, L_I) of a finite plate with an edge crack under tension is examined considering following geometric dimensions and loading conditions (Fig. 8(a)) (Atroshchenko & Bordas, 2015; Diegele et al., 2004):

$$H = 11\,(\text{mm}), \quad L = 20\,(\text{mm}), \quad a = 1\,(\text{mm})$$
$$\sigma_{22}(x_1, L) = -\sigma_{22}(x_1, 0) = \sigma_0 = 100\,(\text{MPa}) \tag{56}$$

Although in the reference studies; Atroshchenko & Bordas, 2015, Diegele et al. 2004, the uniform stress is applied to the crack faces rather than horizontal edges, same values for K_I and L_I should emerge following the principles of superposition (Sun & Jin 2011). In this case, the non-locality is more pronounced compared to previous example as a result of increased characteristic length, l_c, and coupling number, N, allowing us to investigate its effect on the error:

$$E = 100 \times 10^3\,(MPa), \; \nu = 0.3, \; \begin{matrix} l_c = 0.806226\,(mm) \\ l_c/a = 0.806226 \end{matrix}, \; N = 0.849837 \tag{57}$$

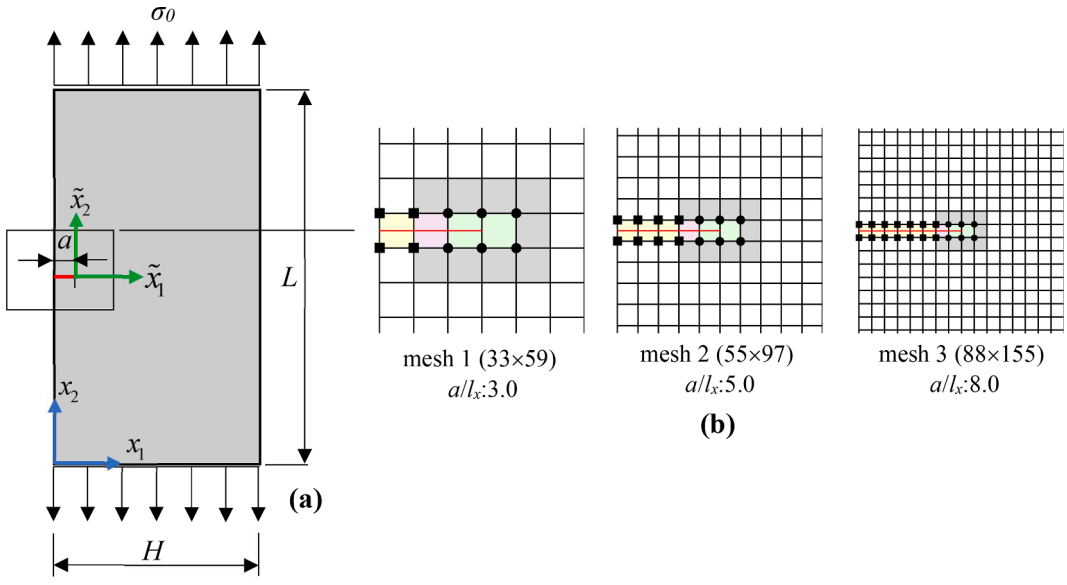

Fig. 8. (a) Schematic of the edge crack model under tension, and (b) corresponding discretization with l_x referring to element length.

As different from previous example, the discretization is arranged to ensure that crack tip lies at the element edge (Fig. 8(b)) which allows us to check the contribution of increased number of crack-tip enriched nodes on the accuracy while the edge crack is located at the middle of left surface to perform the calculations with an altered orientation of local crack tip coordinate system.

The intensity factors are non-dimensionalized as follows where K_I^{local} equals to 208.1 MPa.mm$^{1/2}$ (Tada et al., 2000):

$$\overline{K}_I = \frac{K_I}{K_I^{\text{local}}}, \quad \overline{L}_I = \frac{L_I}{\sigma_0 a\sqrt{\pi a}} \tag{58}$$

The results reported in literature for low, moderate and high non-localities are tabulated in Table 3 while for calculation of relative error (Eq. (55)) the values in Atroshchenko & Bordas, 2015 is utilized as reference since the ones in Diegele et al. 2004 are extracted from the graphs.

From Table 3, it is evident that, the internal characteristic length, l_c, and K_I has an adverse relation: K_I decreases with increasing l_c for a fixed coupling number, N= 0.849837. However, the magnitude of K_I being larger or smaller than the one in the classical theory depends on the ratio between crack size and characteristic length (Li & Lee, 2009), such that for a low level non-locality, $l_c/a \to 0$, micropolar theory yields higher values; $K_I > K_I^{\text{local}}$, whereas for moderate or high level of nonlocalities, we obtain an opposite trend; $l_c/a \to 1$, $l_c/a \geq 1$; $K_I < K_I^{\text{local}}$.

With this knowledge, the effect of discretization and integral domain radius are studied regarding the case of moderate non-locality; l_c/a= 0.806226 for which the variation of intensity factors and relative differences are demonstrated in Fig. 9. The results clearly show the error reducing effect of increased number of crack-tip enriched nodes and elevated non-locality, which is particularly pronounced for CSIF. For instance; compared to L_I of previous example with l_c/a= 0.353553, N= 0.353553, the minimum error, that are attained for the smallest integral radius, is decreased from 5.20 %, 3.20 %, 0.98 % to 1.78 %, 0.08 % and 0.02 % for different meshes. Moreover, in parallel with the previous findings, L_I has higher dependency on the discretization compared to the K_I for which no significant difference in terms of accuracy is attained compared to Griffith problem. Nevertheless, for both parameters, the results tend to approach to ones in reference study as the mesh becomes more refined, such that the error is reduced from 0.60 % to 0.00 % for K_I, and from 1.78 % to 0.02 % for L_I. Consequently, the trend of the errors, once again verifies the capability of combined micropolar/XFEM model which ensures precise results that are achievable even with a coarse mesh configuration.

3.1.3. *Finite plate with an edge crack under shear*

As the last step of validation test, a finite micropolar crack with an edge crack under shear is studied (Fig. 10). The dimensions and material properties are the same as previous example examined in Section 3.1.2, while following loading and boundary conditions are applied to mimic the Mode II case:

$$\begin{aligned} &\tau_{12}(x_1, L) = -\tau_{12}(x_1, 0) = \tau_{21}(H, x_2) = -\tau_{21}(0, x_2) = \tau_0 = 100\,(\text{MPa}) \\ &u_1(0,0) = u_2(0,0) = 0 \end{aligned} \tag{59}$$

As the couple-stress field does not contain any singular term (L_{II}: non-exist see Eq. $(7)_2$), only the value of SIF for Mode II; K_{II}, that is obtained for different non-localities are non-dimensionalized by dividing it with the local case:

$$\overline{K}_{II} = \frac{K_{II}}{K_{II}^{\text{local}}}, \quad K_{II}^{\text{local}} = 199.3\,\text{MPa}\,\text{mm}^{1/2} \tag{60}$$

The K_{II} values reported in literature for low, moderate and high non-localities are listed in Table 4. From the results, it can be deduced that, an increase in non-locality through characteristic length for a fixed coupling number always reduces the K_{II}, while its value being higher or lower than the classical case depends on the ratio between crack and the characteristic length, similar to Mode I case. Nevertheless, the K_{II} turn out to be higher than the ones obtained for Mode I case considering same material parameters.

In the light of these information, the $\overline{K}_{II}$ values, that are obtained by the developed micropolar/XFEM model regarding various non-localities and *I/J-integral* radius (see Table 5) are commented on. Once again, for comparison, the values in Atroshchenko & Bordas, 2015 are utilized as reference, since the ones in Diegele et al. 2004 are extracted from the graphs.

Table 5 shows that as $r_{I,}$ increases, K_{II} converges to a fixed value, the error of which decreases with pronounced non-locality in accordance with Mode I case. For instance; a difference of 3.31 %, 1.08 % and 0.87 % with reference study is obtained for low, moderate and high non-localities. Nevertheless, the trend and level of error are slightly different from the ones in Mode I case for increased r_I. This variation can be attributed to the differences in loading and boundary conditions between reference and present studies; in Atroshchenko & Bordas, 2015, the shear stress is applied at the crack surfaces with fixing the node at the right edge, whereas

Table 3
Fracture parameters reported in literature for a finite micropolar plate with an edge crack under tension.

Reference	Method	l_c (mm)	$\overline{K}_I$	$\overline{L}_I$
Diegele et al., 2004	Standard finite element method	0.254951	1.0796	-0.2211
		0.806226	0.9582	-0.3850
		2.549510	0.8834	-0.4845
Atroshchenko & Bordas, 2015	Standard boundary element method	0.254951	1.0803	-0.2120
		0.806226	0.9542	-0.3689
		2.549510	0.8836	-0.4644

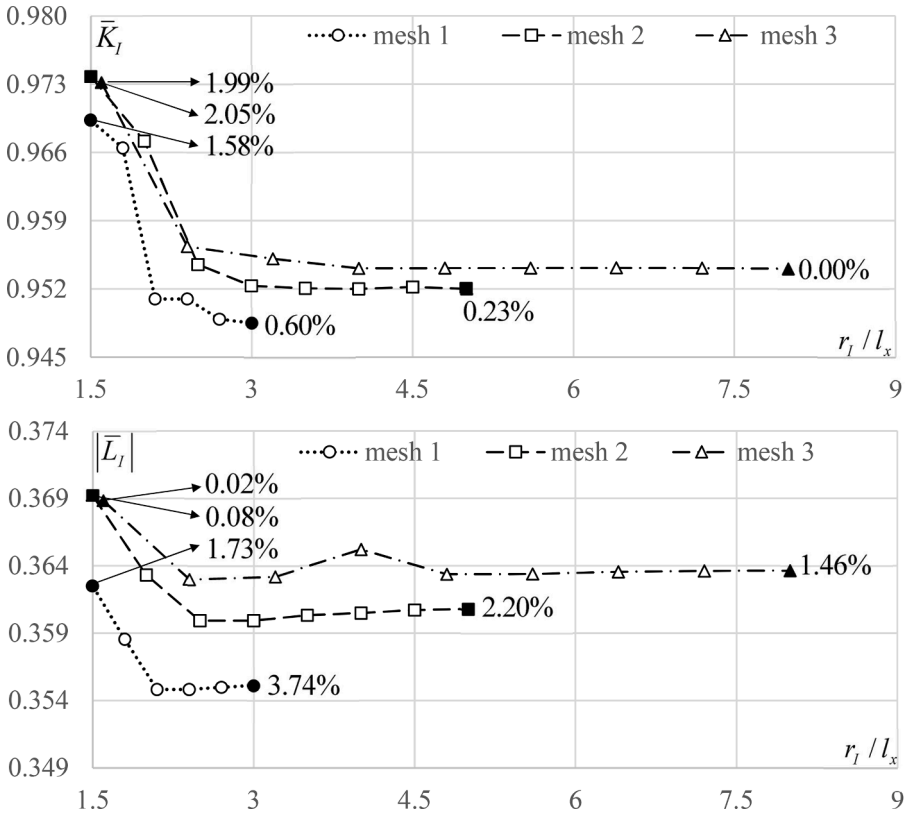

Fig. 9. Variation of fracture parameters obtained by the present micropolar/XFEM model for edge crack problem under uniform tension with moderate non-locality ($l_c = 0.806226$, $N = 0.849837$) regarding various element size, l_x, and domain radius (r_I/l_x), with the relative errors calculated with respect to Atroshchenko & Bordas, 2015.

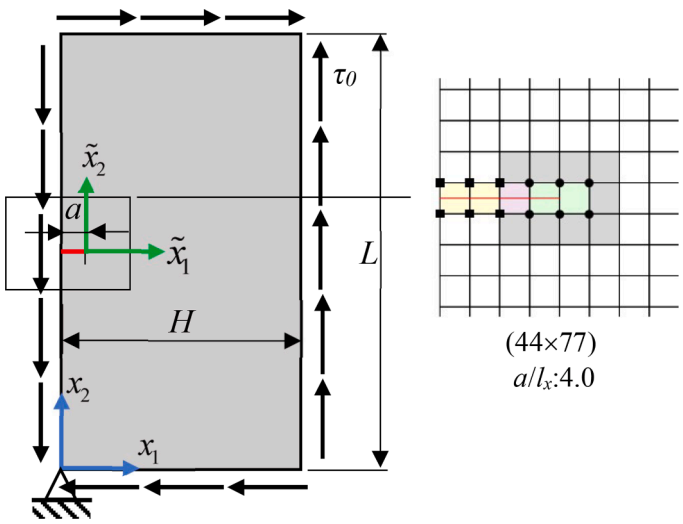

Fig. 10. Schematic of the edge crack model under shear and corresponding discretization with l_x referring to element length.

Table 4
Fracture parameter reported in literature for edge crack problem under shear.

Reference	Method	l_c (mm)	$\overline{K}_{II}$
Diegele et al., 2004	Standard FEM	0.254951	1.2272
		0.806226	1.0154
		2.549510	0.9222
Atroshchenko & Bordas, 2015	Standard BEM	0.254951	1.2241
		0.806226	1.0175
		2.549510	0.9194

here the configuration is arranged as shown in Fig. 10.

Before any further progress, it should be noted that, up to now, the versatility of the XFEM is investigated through plates containing a straight crack that is parallel to horizontal edges of the domain for which a very high accuracy is obtained without the need to increase the number of sub-quads. Nevertheless, one should realize that in case of oblique cracks, the level of error might increase due to inevitable splitting of some sub-quads containing the crack as highlighted in yellow in Fig. 6.

In overall, from the results of validation studies, we believe that, our claim on proposing a numerical methodology that enables researchers to obtain basic fracture parameters of micropolar continuum with sufficient accuracy in a computationally efficient manner (compared to existing approaches in the literature, especially standard FEM) has been actualized through topological enrichment. Although the convergence rate is open to improvement via geometric enrichment, the peculiar character of XFEM, which eliminates the need to have conforming mesh with crack geometry, substantially decreases the number of required elements along and ahead of the crack-tip.

3.2. *Case study: Finite micropolar and cauchy plates with an oblique edge crack under uniform tension*

Present sub-section is devoted on demonstrating the variation of fracture parameters on non-locality. For this purpose, we consider a finite plate under uniform tension having dimensions of $H\times L$ with an edge crack of length $a= 0.4H$ that is located at the middle of left vertical edge making an angle of $\beta = 30^\circ$ with x_1-axis, as illustrated in Fig. 11(a).

$$\begin{aligned} &H = 10\,(\text{mm}), \quad L = 20\,(\text{mm}), \quad a = 4\,(\text{mm}) \\ &\sigma_{22}(x_1, L) = -\sigma_{22}(x_1, 0) = \sigma_0 = 100\,(\text{MPa}) \end{aligned} \tag{61}$$

This is the second example in literature that focuses on the effect of oblique cracks in a micropolar medium within the framework of LEFM (Yu et al., 2014).

As the first step, various sensitivity analyzes are performed considering different mesh configurations (mesh 1: 31 × 63, mesh 2: 39 × 77, mesh 3: 47 × 91 elements, (see Fig. 11(b))), and number of sub-quads (2 × 2, 4 × 4, 8 × 8). In all, the fracture parameters are extracted for various *J/I-integral* domain radii (r_I/l_x = 1.5, 1.8, 2.0, 2.5, 3.0, 3.5, 4.0 with l_x referring to element length along x_1-axis), while non-locality is kept constant at a moderate value:

$$E = 100 \times 10^3\ (\text{MPa}), \quad \nu = 0.3, \quad l_c/a = 0.75\ (l_c = 3\,\text{mm}), \quad N = 0.75 \tag{62}$$

The resulting parameters are non-dimensionalized as follows similar to literature:

$$\overline{K}_I = \frac{K_I}{\sigma_0\sqrt{\pi a}}, \quad \overline{K}_{II} = \frac{K_{II}}{\sigma_0\sqrt{\pi a}}, \quad \overline{L}_I = \frac{L_I}{\sigma_0 a\sqrt{\pi a}}, \quad \overline{u}_0 = u_0\frac{2\mu}{\sigma_0 a}, \quad \overline{G} = \frac{2G}{\pi a(\sigma_0)^2(1-\nu)/\mu} \tag{63}$$

The mesh insensitivity is evident from the left column of graphs in Fig. 12, as the maximum difference between coarsest and finest meshes (mesh 1 vs mesh 3) are 0.15 % (K_I), 0.06 % (K_{II}) and 0.30 % (L_I), for which the number of sub-quads required for numerical integrations of enhanced elements are taken as 4 × 4 and comparison is made through converged values; $r_I/l_x > 2.0$. Similarly, from the sensitivity analyzes of altered number of sub-quads for the model with mesh 2, dividing elements into 2 × 2 or 8 × 8 parts does not lead to any noticeable change with a relative discrepancy of 0.26 % (K_I), 0.22 % (K_{II}) and 0.75 % (L_I).

As the next step, a parametric study is performed to display the influence of non-locality on basic fracture parameters such as; SIFs (K_I, K_{II}), CSIF (L_I), crack opening displacement and ERR (G), in a comprehensive manner. This is achieved by altering the micropolarity

Table 5
Variation of SIF for Mode II; K_{II}, obtained by micropolar/XFEM model for edge crack problem under shear for low, moderate and high non-localities regarding various domain radius (r_I/l_x), reported alongside with the relative errors calculated with respect to Atroshchenko & Bordas, 2015.

	$l_c = 0.254951$ (mm)	$l_c = 0.806226$ (mm)	$l_c = 2.54951$ (mm)
$r = 1.5l_x$	1.2123 (1.21 %)	1.0255 (1.00 %)	0.9332 (1.19 %)
$r = 2.0l_x$	1.2067 (1.67 %)	1.0196 (0.41 %)	0.9275 (0.58 %)
$r = 2.5l_x$	1.1902 (3.01 %)	1.0071 (0.82 %)	0.9165 (0.62 %)
$r = 3.0l_x$	1.1874 (3.24 %)	1.0050 (1.02 %)	0.9147 (0.82 %)
$r = 3.5l_x$	1.1870 (3.27 %)	1.0046 (1.07 %)	0.9143 (0.86 %)
$r = 4.0l_x$	1.1865 (3.31 %)	1.0044 (1.08 %)	0.9142 (0.87 %)

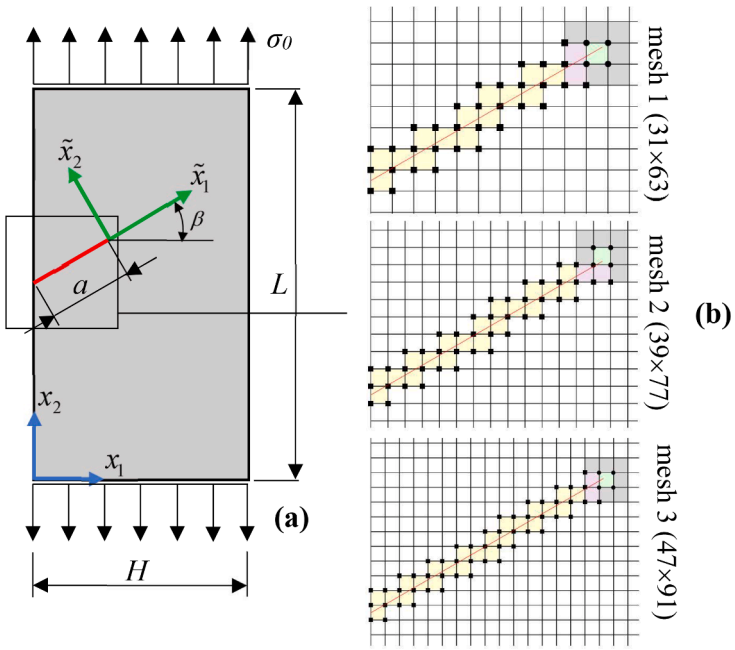

Fig. 11. (a) Schematic of the oblique edge crack model, (b) corresponding discretization.

related material parameters; internal characteristic length, l_c, and coupling number, N, as follows:

$$l_c/a = 0.10a, 0.375a, 0.75a, 1.25a, \quad N = 0.0001, 0.05, 0.15, 0.30, 0.45, 0.60, 0.75, 0.9 \tag{64}$$

All the subsequent simulations are performed for a model discretized by 39 × 77 elements (mesh 2) while for numerical simulation 4 × 4 sub-quads are used following the sensitivity analysis. The opening displacement at crack mouth alongside with SIFs, CSIF, ERR that are extracted for a domain radius of $r_I / l_x = 2.5$ are shown graphically in Fig. 13.

Here the coupling number approaching to zero, $N \to 0$, refers to limiting case of classical elasticity, hence the results should coincide with the ones of Cauchy continuum. This allows us to check the XFEM algorithm for oblique cracks by comparing the SIFs obtained from the in-house code (mesh 2, 4 × 4 sub-quads, $r_I / l_x = 2.5$) by the ones available in literature (Fayed 2016). The data extracted from the plots of reference study for a domain with same geometric dimensions are $\overline{K}_I = 1.54, \ \overline{K}_{II} = 0.47$ according to which the level of error is calculated as 1.09 % and 0.17 %, respectively (Eq. (62)), proving the versatility and accuracy of the presented method once again.

From Fig. 13(a) and (b), it can be deduced that increasing characteristic length, l_c, decreases the SIF(s) for a fixed coupling number, N, while whether the values will be larger or smaller than those obtained for Cauchy continuum depends on the ratio between l_c and a. For non-pronounced non-locality; $l_c/a \to 0$, SIFs of micropolar continuum turns out to be higher than classical ones; $K > K^{\text{local}}$, as coupling number approaches to the upper bound; ($N \to 1$), whereas an opposite trend; $K < K^{\text{local}}$, is obtained for high level non-locality; $l_c/a \to 1$, $l_c/a \geq 1$. Accordingly, we can conclude that, for a micropolar continuum under mixed mode loading, SIF(s) varies depending on not only micropolarity related material parameters (l_c, N), but also the ratio between internal and crack lengths (l_c/a), as previously pointed out by Diegele et al. 2004 and Li & Lee 2009 for Mode I and II cases, separately. The variation of CSIF (Fig. 13(c)), on the other hand, indicates the singularity-enhancing feature of micropolarity as the amplitude of couple-stress singularity elevated with internal characteristic length and coupling number.

Nevertheless, as evident from the decreasing trend of crack opening displacement (Fig. 13(d)), a defected micropolar plate ($l_c, N > 0$) deforms less than its Cauchy counterpart under same conditions, while the rigidity becomes even more pronounced with increasing material parameters, $l_c \uparrow, \ N \uparrow$, as illustrated in Fig. 14. Finally, the case study clearly reveals the opposite correlation between non-locality and ERR (Fig. 13(e)), such that higher the non-locality, lower the *driving force* which is responsible for promoting crack propagation. This finding suggests that non-locality (or presence of microrotations) reduces the effects of defects (cracks, holes) as stress concentrator in scale-dependent plates as in accordance with the available literature (Atkinson & Leppington, 1977; Paul & Sridharan, 1981; Shmoylova et al., 2007; Tuna et al., 2020; Tuna & Trovalusci, 2021). Note that, the ERR values reported herein are obtained through numerical derivation of *J-integral*, whereas it can alternatively be calculated by substituting SIFs and CSIF in Eq. (13). At this point, it should once again be mentioned that, in Kapiturova et al. 2016, which can be considered as an noticeable attempt in exploiting XFEM for brittle fracture analysis of micropolar solids, the trend between ERR (driving force) and non-locality does not agree with the present study and literature. This point is further examined by comparing the J-integral values obtained via the presented micropolar/XFEM model with the ones given in Kapiturova et al. 2016 (see Figs. 8 and 9 in the reference study) regarding the domain with an edge crack under tensile loading. As different from the referenced study, the value of J-integral has a decreasing trend

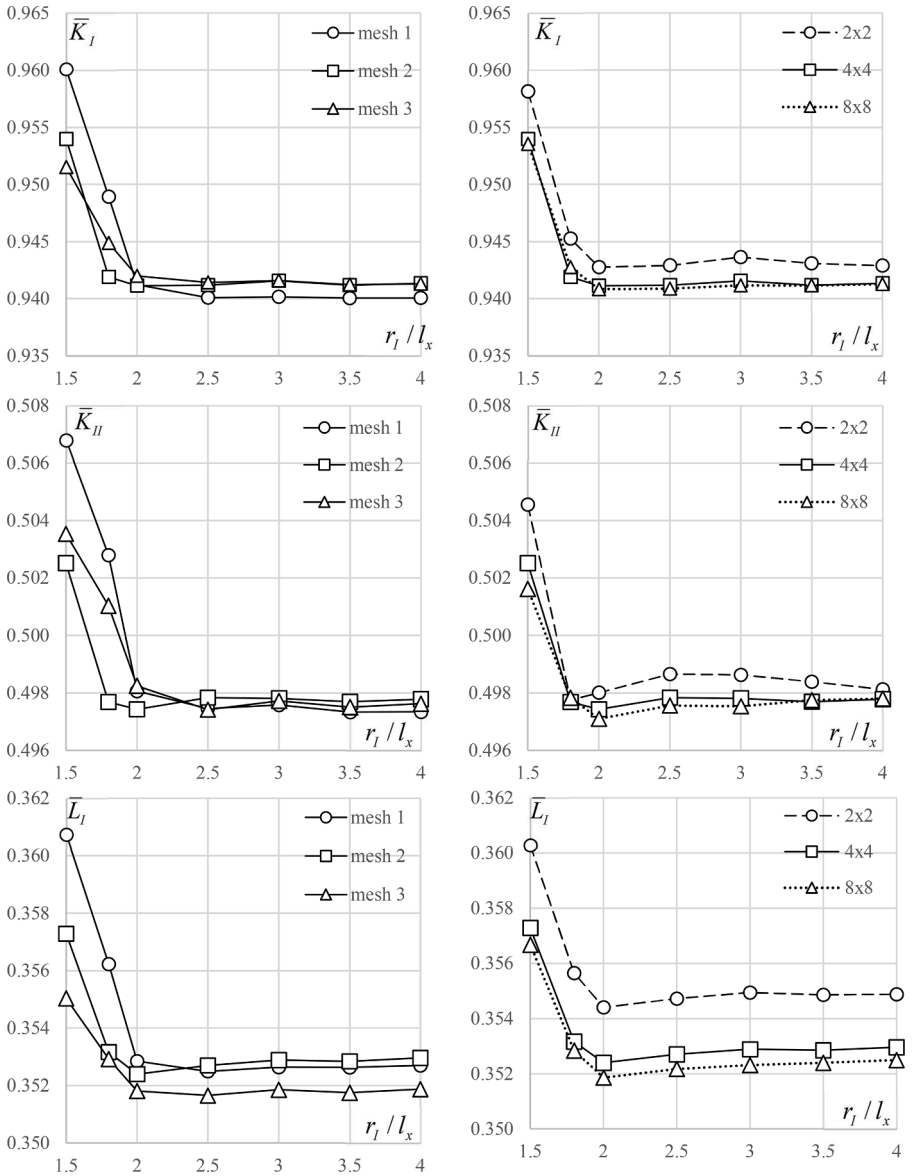

Fig. 12. Sensitivity analyzes for micropolar plate with an oblique edge crack under uniform tension: variation of fracture parameters; mode I SIF (first row), Mode II SIF (second row), Mode I CSIF (third row) with various domain radius (r_I) considering different mesh configurations; mesh 1, mesh 2, mesh 3 (left column) and different number of sub-quads; 2 × 2, 4 × 4, 8 × 8 (right column).

with increased coupling number. For instance; for the case where crack equals to half of the width and coupling number is $N \cong 0.845$, the J-integral is reduced about 6 % compared to the Cauchy case, whereas in Kapiturova et al. 2016, an increase of 16 % is obtained.

As the last step of this sub-section, the influence of crack size on the variation of fracture parameters are studied by performing additional simulations with distinct crack lengths while material parameters are fixed:

$$a = 2, 3, 4, 5, 6\,(\text{mm})$$
$$E = 100 \times 10^3\ (\text{MPa}), \quad \nu = 0.3, \quad l_c = 3\,(\text{mm}), \quad N = 0.75 \tag{65}$$

The analyzes are repeated for Cauchy continuum to make a comparison with the local case, while the results, that are extracted for mesh 2, 4 × 4 sub-quads and a domain radius of $r_I / l_x = 2.5$, are demonstrated in Fig. 15. One should realize that since the material parameters are fixed, the ratio between internal and crack lengths is decreased from $l_c / a = 1.5$ to $l_c / a = 0.5$ as the size of crack is tripled. For both continua, an increase in crack length leads the structure to become more prone to fracture type failure whereas for the micropolar continuum this variation seems to be less dramatic than the Cauchy one.

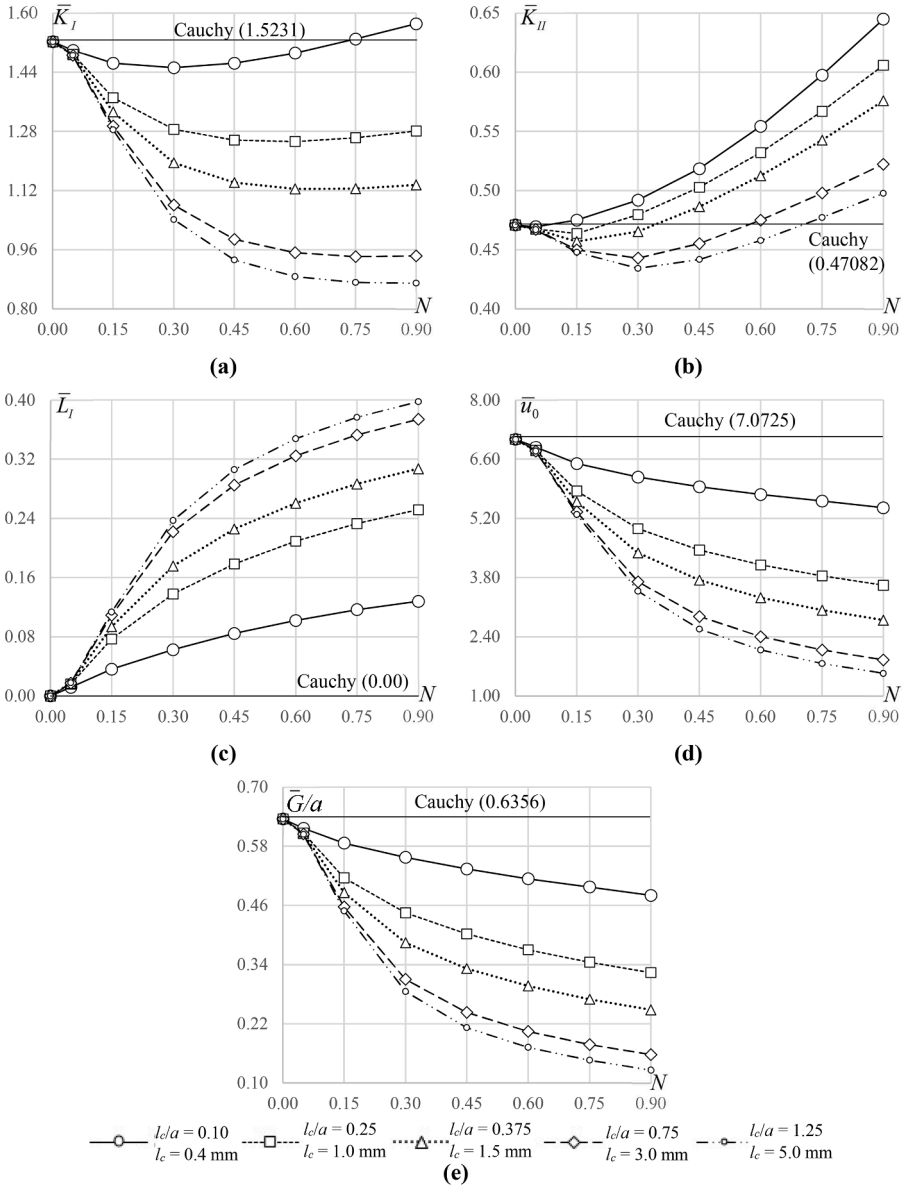

Fig. 13. Parametric study for micropolar plate with an oblique edge crack under uniform tension: variation of fracture parameters; Mode I SIF (a), Mode II SIF (b), Mode I CSIF (c), opening displacement at crack mouth (d), and ERR (e), with coupling number, N, and internal characteristic length, l_c whereas straight black line indicate the results of Cauchy continuum.

4. Discussion

The micropolar/XFEM model, that is built for computationally efficient extraction of basic fracture parameters required within LEFM framework, has been validated, and employed to investigate the case with an oblique edge crack. Though, the analyzes have targeted domains with stationary (non-propagating) cracks so far, the model can be directly exploited to simulate the evolution of damage by simply adapting an iterative loop. Owing to ability of XFEM, eliminating re-meshing process, the crack evolution can be traced within a fixed domain discretization. However, the approach has a drawback: an explicitly defined fracture criterion should be introduced to calculate the propagation angles forming the crack path, which is still an open issue for micropolar continuum.

Therefore, despite all its potential, the LEFM based numerical models (Atroshchenko & Bordas, 2015; Diegele et al., 2004; Yu et al., 2014) have not been used for this purpose, and other approaches such as phase field (Behera et al., 2024; Suh et al., 2020; Riad et al., 2022), and peridynamics (Chen et al., 2024; Diana et al., 2024; Guo et al., 2024; Lei et al., 2024; Wan et al., 2022; Zhou et al., 2023) have been extended to simulate the crack propagation. Both methodologies provide significant insight on the topic, each with their own advantageous: in the phase field method, propagation phenomenon is simply governed by minimizing the defined energy

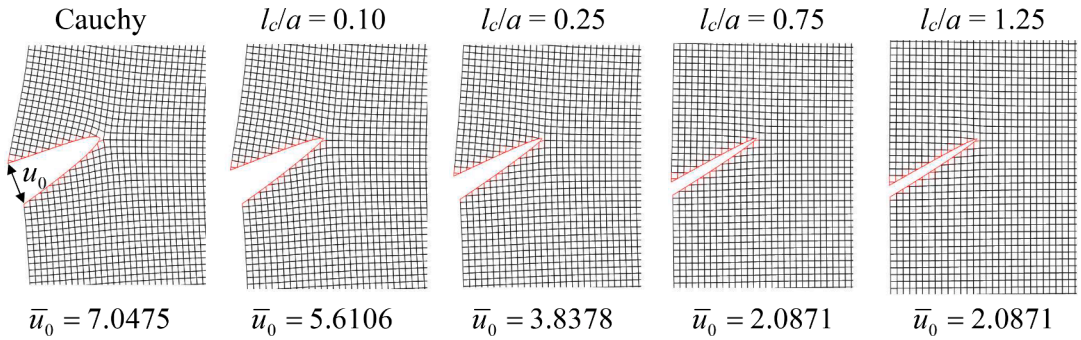

Fig. 14. Variation of deformed configurations (exaggerated 50 times) for a coupling number of N= 0.75 and various characteristic lengths.

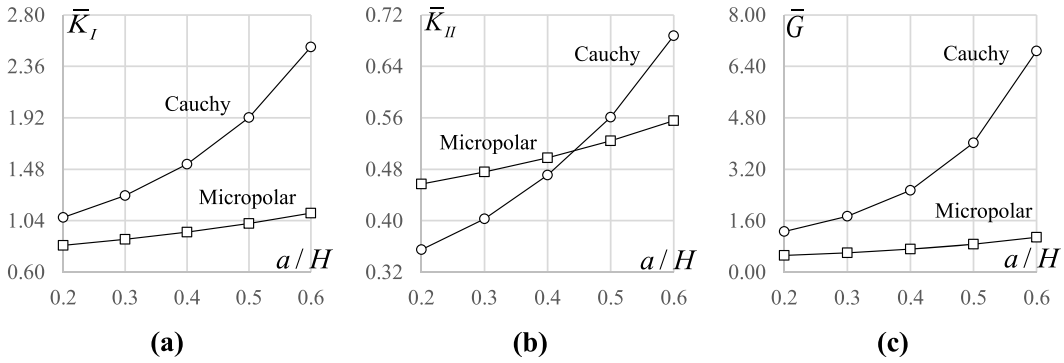

Fig. 15. Parametric study for Cauchy and micropolar plates with an edge crack under uniform tension: Variation of Mode I SIF (a), Mode II SIF (b), and ERR (c) for various crack lengths, a, considering a fixed domain ($H\times L$) and constant material parameters (l_c = 3 mm, N= 0.75).

functional in which the dissipative and dynamical effects can be easily incorporated, while in peridynamics, the interactions between material points located within a finite neighbourhood are explicitly covered which inherently eliminates the need to have an external failure criterion, and overcomes the shortcoming of crack-tip singularity. Though both approaches suggest realistic predictions for fracture problems, their limitations should be recognized. For instance; in phase field method, the need to having a regularization length smaller than the internal length parameter, and a finite element discretization smaller than the regularization parameter, increases the computational cost (Riad et al., 2022). Moreover, regarding the obtained crack paths, it is highlighted that, a universal decomposition scheme that is applicable under all loading conditions is still missing (Behera et al., 2024). As for peridynamics, the main challenge arises in computational sense due to non-local nature of the problem for which the effect of material point density and horizon size should be studied (Diana et al., 2024; Guo et al., 2024). Moreover, in case of bond-based peridynamics, a more realistic criterion than critical elongation should be defined due to presence of particle rotations (Lei et al., 2024; Wan et al., 2022). Lastly, some differences are encountered in terms of crack paths and their variation with micropolar material parameters, indicating the lack of consensus (Behera et al., 2024; Chen et al., 2024; Suh et al., 2020).

All these above-referred facts point out that the topic is still open for further investigations. To this end, the presented micropolar/XFEM model, which can be exploited in proposal and validation of a fracture criterion within LEFM approach (Tuna et al., 2024), forms the basis to investigate crack growth phenomenon, and to simulate the corresponding damage process, in a computationally efficient manner within the framework of LEFM.

5. Conclusions and further developments

The main aim of this paper is to build a computationally efficient numerical model by implementing extended finite element method to two-dimensional micropolar structures (i.e. micropolar/XFEM model) through which the basic fracture parameters required in linear elastic fracture mechanics (LEFM) can be extracted easily. The model provides the basis to explore the crack propagation phenomenon within the framework of LEFM, an approach exploited only for domains with stationary cracks so far, due to numerical challenges, and the absence of a valid fracture criterion.

The accuracy of formulation and in-house code is verified by comparing stress and couple-stress intensity factors (SIFs and CSIF) obtained through the micropolar/XFEM model with the ones reported in literature considering Mode I (crack opening) and Mode II (crack shearing) cases. As evident from the errors given for various discretizations, the current form of the developed formulation provides reliable outputs in a computationally efficient manner due to the peculiar character of XFEM that eliminates the need to have

a conforming mesh with crack geometry, and substantially decreases the number of required elements along and ahead of the crack-tip.

Following its versatility, persistent even for a coarse mesh discretization, the analyzes are extended to study the contribution of scale effects on the integrity assessment of a micropolar plate with an oblique edge crack. The results highlight the significance of correct representation of materials with microstructure since an increase in non-locality is proved to reduce the effect of defects (e.g. cracks, holes) as stress concentrators following the decreased trend of energy release rate and deformation state.

By considering its accuracy and efficiency for size-dependent fracture problems and great potential on numerical simulation of damage process, the micropolar/XFEM model can be exploited in proposal and validation of a fracture criterion within LEFM approach, which is, in fact, the scope of a forthcoming paper of the Authors, and offers a new and different perspective to available methods (e.g. phase field, peridynamics).

CRediT authorship contribution statement

Meral Tuna: Writing – review & editing, Writing – original draft, Validation, Methodology, Investigation, Conceptualization. **Patrizia Trovalusci:** Writing – review & editing, Supervision, Project administration, Investigation, Funding acquisition, Conceptualization. **Nicholas Fantuzzi:** Writing – review & editing, Supervision, Project administration, Investigation, Funding acquisition, Conceptualization.

Declaration of competing interest

The authors declare that they have no known competing financial interests or personal relationships that could have appeared to influence the work reported in this paper.

Acknowledgments

The Authors acknowledge the support of PRIN 2020, Project 2020F23HZ7_003 (J35F22000640001), PRIN 2022, Project 2022YLNJRY (J53D23002500006) Funded by the European Union – Next Generation EU, Ministry of University of Research (MUR), and PNRR CN1 – Spoke 6 (B83C22002940006).

Appendix A

$$P^{(a,r)}_{i1,i} = \underbrace{\left(C_{mnpr}\varepsilon^a_{pr}\varepsilon_{mn} + D_{m3p3}\chi^a_{p3}\chi_{m3}\right)_{,1}}_{[1]} - \underbrace{\left(\sigma^a_{ij}u_{j,1} + \sigma_{ij}u^a_{j,1} + \mu^a_{i3}\phi_{3,1} + \mu_{i3}\phi^a_{3,1}\right)_{,i}}_{[2]} \tag{A.1}$$

Let's start with [1]:

$$C_{mnpr,1}\varepsilon^a_{pr}\varepsilon_{mn} + C_{mnpr}\varepsilon^a_{pr,1}\varepsilon_{mn} + \sigma^a_{mn}\varepsilon_{mn,1} + D_{m3p3,1}\chi^a_{p3}\chi_{m3} + D_{m3p3}\chi^a_{p3,1}\chi_{m3} + \mu^a_{m3}\chi_{m3,1} \tag{A.2}$$

Following the homogeneity of the medium, the terms containing $C_{mnpr,1}$ and $D_{m3p3,1}$ dies out, while substitution of the kinematic relations to the resulting expression gives:

$$\sigma_{ij}u^a_{j,i1} + \sigma^a_{ij}\left(u_{j,i1} - \varepsilon_{ij3}\phi_{3,1}\right) + \mu_{i3}\phi^a_{3,i1} + \mu^a_{i3}\phi_{3,i1} \tag{A.3}$$

Now as for the [2]:

$$\sigma^a_{ij,i}u_{j,1} + \sigma^a_{ij}u_{j,i1} + \sigma_{ij,i}u^a_{j,1} + \sigma_{ij}u^a_{j,i1} + \mu^a_{i3,i}\phi_{3,1} + \mu^a_{i3}\phi_{3,i1} + \mu_{i3,i}\phi^a_{3,1} + \mu_{i3}\phi^a_{3,i1} \tag{A.4}$$

Here the terms including $\sigma^a_{ij,i}$, $\sigma_{ij,i}$ and $\mu^a_{i3,i}$ vanishes following the equilibrium equations, and the substitution of the equilibrium equation for the real couple-stress field results in:

$$\sigma^a_{ij}u_{j,i1} + \sigma_{ij}u^a_{j,i1} + \mu^a_{i3}\phi_{3,i1} - \varepsilon_{3ij}\sigma_{ij}\phi^a_{3,1} + \mu_{i3}\phi^a_{3,i1} \tag{A.5}$$

Finally, from Eqs. (A.1); (A.3); (A.5), we have:

$$P^{(a,r)}_{i1,i} = \varepsilon_{ij3}\left(\sigma_{ij}\phi^a_{3,1} - \sigma^a_{ij}\phi_{3,1}\right) \tag{A.6}$$

Data availability

Data will be made available on request.

References

Altenbach, H., & Eremeyev, V. (2012). Generalized Continua - from the theory to engineering applications. *CISM international centre for mechanical sciences*. Vienna: Springer.

Atkinson, C., & Leppington, F. (1977). The effect of couple stresses on the tip of a crack. *International Journal of Solids and Structures, 13*, 1103–1122.

Atroshchenko, E., & Bordas, S. P. A. (2015). Fundamental solutions and dual boundary element methods for fracture in plane Cosserat elasticity. *Proceedings of the Royal Society A: Mathematical, Physical and Engineering Sciences, 471*, Article 20150216.

Barenblatt, G. I. (1962). The mathematical theory of equilibrium cracks in brittle fracture. *Advances in Applied Mechanics, 7*, 55–129.

Barretta, R., Faghidian, S. A., & Marotti de Sciarra, F. (2024). Stress-driven nonlocal integral elasticity for axisymmetric nano-plates. *International Journal of Engineering Science, 136*, 38–52.

Béchet, E., Minnebo, H., Moës, N., & Burgardt, B. (2005). Improved implementation and robustness study of the X-FEM for stress analysis around cracks. *International Journal for Numerical Methods in Engineering, 64*, 1033–1056.

Behera, A. K., Das, A., & Rahaman, M. M. (2024). Two different micro-polar phase-field models for brittle fracture and their open-source finite element implementation. *Engineering Fracture Mechanics, 295*, Article 109782.

Belytschko, T., & Black, T. (1999). Elastic crack growth in finite elements with minimal remeshing. *International Journal for Numerical Methods in Engineering, 45*, 601–620.

Belytschko, T., Gracie, R., & Ventura, G. (2009). A review of extended/generalized finite element methods for material modelling. *Modelling and Simulation in Materials Science and Engineering, 17*, Article 043001.

Benvenuti, E., Orlando, N., Ferretti, D., & Tralli, A. (2016). A new 3D experimentally consistent XFEM to simulate delamination in FRP-reinforced concrete. *Composites Part B, 91*, 346–360.

Berkache, K., Phani, S., & Ganghoffer, J.-F. (2022). Micropolar effects on the effective elastic properties and elastic fracture toughness of planar lattices. *European Journal of Mechanics - A/Solids, 93*, Article 104489.

Capriz, G. (1989). Continua with Microstructure. *Springer tracts in natural philosophy*. Springer-Verlag.

Chahine, E., Laborde, P., & Renard, Y. (2006). A quasi-optimal convergence result for fracture mechanics with XFEM, Comptes rendus de l'Académie des sciences. *Série I, Mathématique,, 342*, 527–532.

Chen, F. H. K., & Shield, R. T. (1977). Conservation laws in elasticity of the J-integral type. *Zeitschrift für angewandte Mathematik und Physik, 28*, 1–22.

Chen, Z., Chu, X., & Yang, D. (2024). A Cosserat bond-based correspondence model and the investigation of microstructure effect on crack propagation. *Computational Particle Mechanics*. https://doi.org/10.1007/s40571-024-00785-0

Cherepanov, G. P. (1967). The propagation of cracks in a continuous medium. *Journal of Applied Mathematics and Mechanic, 31*, 503–512.

Chessa, J., Wang, H., & Belytschko, T. (2003). On the construction of blending elements for local partition of unity enriched finite elements. *International Journal for Numerical Methods in Engineering, 57*, 1015–1038.

Chroni, E., Bakalakos, S., Sotiropoulos, G., & Papadopoulos, V. (2024). Topology optimization of bi-material structures with Iso-XFEM. *Composite Structures, 331*, Article 117902.

Colatosti, M., Fantuzzi, N., & Trovalusci, P. (2021). New insights on homogenization for hexagonal-shaped composites as Cosserat continua. *Meccanica, 57*, 885–904.

Cosserat, E., & Cosserat, F. (1909). *Théorie des corps déformables*. Paris: Herman et fils.

Daux, C., Moes, N., Dolbow, J., Sukumar, N., & Belytschko, T. (2000). Arbitrary cracks and holes with the extended finite element method. *International Journal for Numerical Methods in Engineering, 48*, 1741–1760.

Deng, H., Yan, B., Zhang, X., & Zhu, Y. (2022). A new enrichment scheme for the interfacial crack modelling using XFEM. *Theoretical and Applied Fracture Mechanics, 122*, Article 103595.

Deng, H., Yan, B., Zhang, X., Zhu, Y., & Koyanagi, J. (2023). New crack front enrichment for XFEM modelling. *International Journal of Solids and Structures, 274*, Article 112280.

Diana, V., Bacigalupo, A., & Gambarotta, L. (2024). Continuum-molecular modeling of planar micropolar media: Anisotropy, chiral properties and length-scale effects. *International Journal of Solids and Structures, 295*, Article 112810.

Diegele, E., Elsaber, R., & Tsakmakis, C. (2004). Linear micropolar elastic crack-tip fields under mixed mode loading conditions. *International Journal of Fracture, 129*, 309–339.

Dolbow, J. (1999). *An extended finite element method with discontinuous enrichment for applied mechanics*. Evanston, IL, USA: Theoretical and Applied Mechanics, Northwestern University. Ph.D. thesis.

Dong, J. J., Xu, L., Yu, H. J., Wang, J. S., & Qin, Q. H. (2022). Fracture analysis of chiral fiber-reinforced biocomposite. *Engineering Fracture Mechanics, 271*, Article 108625.

Dyskin, A. V., & Pasternak, E. (2015). Asymtotic analysis of fracture propagation in materials with rotating particles. *Engineering Fracture Mechanics, 150*, 1–18.

Eringen, A. (1999). *Microcontinuum field theory*. Springer.

Eshelby, J. D. (1974). The calculation of energy release rates. editor. In G. C. Sih (Ed.), *Conference on Prospects of Advanced Fracture Mechanics*.

Farajpour, A., Howard, C. Q., & Robertson, W. S. P. (2020). On size-dependent mechanics of nanoplates. *International Journal of Engineering Science, 156*, Article 103368.

Fayed, A. S. (2016). Numerical analysis of mixed mode I/II stress intensity factors of edge slant cracked plates. *Engineering Solid Mechanics, 5*, 61–70.

Fleming, M., Chu, Y. A., Moran, B., & Belytschko, T. (1997). Enriched element-free Galerkin methods for crack tip fields. *International Journal for Numerical Methods in Engineering, 40*, 1483–1504.

Forest, S., & Sab, K. (1998). Cosserat overall modelling of heterogeneous materials. *Mechanics Research Communications, 25*, 449–454.

Fries, T. P. (2008). A corrected XFEM approximation without problems in blending elements. *International Journal for Numerical Methods in Engineering, 75*, 503–532.

Fries, T. P., & Belytschko, T. (2010). The extended/generalized finite element method: An overview of the method and its applications. *International Journal for Numerical Methods in Engineering, 84*, 253–304.

Garajeu, M., & Soós, E. (2003). Cosserat models versus crack propagation. *Mathematics and Mechanics of Solids, 8*, 189–218.

Gdoutos, E. (2006). *Fracture mechanics: An introduction, solid mechanics and its applications*. Netherlands: Springer.

Ghayesh, M. H., & Farajpour, A. (2019). A review on the mechanics of functionally graded nanoscale and microscale structures. *International Journal of Engineering Science, 137*, 8–36.

Gracie, R., Wang, H., & Belytschko, T. (2008). Blending in the extended finite element method by discontinuous Galerkin and assumed strain methods. *International Journal for Numerical Methods in Engineering, 74*, 1645–1669.

Griffith, A. A. (1921). The phenomena of rupture and flow in solids. *Philosophical Transactions of the Royal Society of London Series A, 221*, 163–198.

Guo, X., Chu, X., & Li, S. (2024). A Cosserat peridynamic model with Bresler-Pister criterion and numerical simulation of concrete fracture. *Acta Mechanica, 235*, 1715–1735.

Gupta, V., Duarte, C. A., Babuška, I., & Banerjee, U. (2013). A stable and optimally convergent generalized FEM (SGFEM) for linear elastic fracture mechanics. *Computer Methods in Applied Mechanics and Engineering, 266*, 23–39.

Gurtin, M. (1999). *Configurational forces as basis concept of continuum physics*. Springer-Verlag.

Huang, R., Sukumar, N., & Prevost, J. H. (2003). Modelling quasi-static crack growth with the extended finite element method Part II: Numerical applications. *International Journal of Solids and Structures, 40*, 7539–7552.

Inglis, C. (1913). Stresses in a plate due to the presence of cracks and sharp corners. *SPIE Milestone Series, 137*, 3–17.

Irwin, G. R. (1948). *Fracture dynamics, fracturing of metals* (pp. 147–166). Cleveland: American Society for Metals.

Irwin, G. R. (1957). Analysis of stresses and strains near the end of a crack traversing a plate. *Journal of Applied Mechanics, 24*, 361–364.

Irwin, G. R. (1968). Linear fracture mechanics, fracture transition, and fracture control. *Engineering Fracture Mechanics, 1*, 241–257.

Jaric, J. (1990). The energy release rate and the J-integral in nonlocal micropolar field theory. *International Journal of Engineering Science, 28*, 1303–1313.
Jasiuk, I., & Ostoja-Starzewski, M. (2004). *From lattices and composites to micropolar continua, 175* p. 212). Dordrecht: Springer Netherlands.
Kachanov, M. (2022). Effective properties of heterogeneous materials as functions of contrast between properties of constituents. *Mathematics and Mechanics of Solids*. https://doi.org/10.1177/10812865221136236
Kachanov, M., & Argatov, I. (2023). The elasticity-conductivity connection for materials with cracks of arbitrary shapes and orientation distributions. *International Journal of Engineering Science, 193*, Article 103958.
Kanaun, S., Markova, I., & Jarillo, G. R. (2023). Effective elastic properties and wave surfaces of rock materials containing multiple cavities and cracks (effective field approach). *International Journal of Engineering Science, 182*, Article 103783.
Kapiturova, M., Gracie, R., & Potapenko, S. (2016). Simulation of cracks in a Cosserat medium using the extended finite element method. *Mathematics and Mechanics of Solids, 21*, 621–635.
Karami, B., Shahsavari, D., Janghorban, M., & Li, L. (2019). On the resonance of functionally graded nanoplates using bi-Helmholtz nonlocal strain gradient theory. *International Journal of Engineering Science, 144*, Article 103143.
Kunin, I. (1984). On foundations of the theory of elastic media with microstructure. *International Journal of Engineering Science, 22*, 969–978.
Kushch, V. I., Shmegera, S. V., & Sevostianov, I. (2009). SIF statistics in micro cracked solid: Effect of crack density, orientation and clustering. *International Journal of Engineering Science, 47*, 192–208.
Laborde, P., Pommier, J., Renard, Y., & Salaün, M. (2005). High-order extended finite element method for cracked domains. *International Journal for Numerical Methods in Engineering, 64*, 354–381.
Lakes, R. (1995). Experimental methods for study of Cosserat elastic solids and other generalized continua. In H. Muhlhaus (Ed.), *Continuum models for materials with micro-structure* (pp. 1–22). New York: Wiley.
Lei, J., Lu, Y., Sun, Y., & Jiang, S. (2024). A micropolar damage model for size-dependent concrete fracture problems and crack propagation simulated by PDDO method. *Engineering Analysis with Boundary Elements, 167*, Article 105882.
Li, Y. D., & Lee, K. Y. (2009). Fracture analysis in micropolar elasticity: Mode-I crack. *International Journal of Fracture, 156*, 179–184.
Lubarda, V. A., & Markenscoff, X. (2003). On conservation integrals in micropolar elasticity. *Philosophical Magazine, 83*, 1365–1377.
Markov, A., & Kanaun, S. (2014). An efficient homogenization method for elastic media with multiple cracks. *International Journal of Engineering Science, 82*, 205–221.
Markov, A., Levin, V., & Markov, M. (2024). Effects of the orientation distribution of thin soft inclusions on the effective moduli of microheterogeneous materials. *International Journal of Engineering Science, 194*, Article 103975.
Masiani, R., & Trovalusci, P. (1996). Cosserat and Cauchy materials as continuum models of brick masonry. *Meccanica, 31*, 421–432.
Maugin, G. (1993). *Material inhomogeneities in elasticity, applied mathematics*. Taylor & Francis.
Melenk, J. M., & Babuska, I. (1996). The partition of unity finite element method: Basic theory and applications. *Computer Methods in Applied Mechanics and Engineering, 139*, 289–314.
Mindlin, R. D. (1964). Micro-structure in linear elasticity. *Archive for Rational Mechanics and Analysis, 16*, 51–78.
Moes, N., Dolbow, J., & Belytschko, T. (1999). A finite element method for crack growth without remeshing. *International Journal for Numerical Methods in Engineering, 46*, 131–150.
Mühlhaus, H. B., & Pasternak, E. (2002). Path independent integrals for cosserat continua and application to crack problems. *International Journal of Fracture, 113*, L21–L26.
Niktitin, E., & Zubov, L. M. (1998). Conservation laws and conjugate solutions in the elasticity of simple materials and materials with couple stress. *Journal of Elasticity, 51*, 1–22.
W. Nowacki (1986) Theory of asymmetric elasticity, Elsevier Science & Technology.
Orowan, E. (1949). Fracture and strength of solids. *Reports on Progress in Physics, 12*, 185.
Paul, H., & Sridharan, K. (1981). The problem of a Griffith crack in micropolar elasticity. *International Journal of Engineering Science, 19*, 563–579.
Ponnusami, S. A., Turteltaub, S., & van der Zwaag, S. (2015). Cohesive zone modelling of crack nucleation and propagation in particulate composites. *Engineering Fracture Mechanics, 149*, 170–190.
Pucci, E., & Saccomandi, G. (1990). Symmetries and conservation laws in micropolar elasticity. *International Journal of Engineering Science, 28*, 557–562, 1990.
Qian, G., Gonzalez-Albuixech, V. F., Niffenegger, M., & Giner, E. (2016). Comparison of KI calculation methods. *Engineering Fracture Mechanics, 156*, 52–67.
Riad, S., Bardel, D., & Rethore, J. (2022). Effect of microstructural length scales on crack propagation in elastic Cosserat media. *Engineering Fracture Mechanics, 267*, Article 108399.
Rice, J. R. (1968). A path independent integral and the approximate analysis of strain concentration by notches and cracks. *Journal of Applied Mechanics, 35*, 379–386.
Shmoylova, E., Potapenko, S., & Rothenburg, L. (2007). Boundary element analysis of stress distribution around a crack in plane micropolar elasticity. *International Journal of Engineering Science, 45*, 199–209.
Sokolowski, M. (1972). *Theory of couple-stresses in bodies with constrained rotations. course and lectures cism*. Springer-Verlag.
Stempin, P., Pawlak, T. P., & Sumelka, W. (2023). Formulation of non-local space-fractional plate model and validation for composite micro-plates. *International Journal of Engineering Science, 192*, Article 103932.
Stern, M., Becker, E. B., & Dunham, R. S. (1976). A contour integral computation of mixed-mode stress intensity factors. *International Journal of Fracture, 12*, 359–368.
Sternberg, E., & Muki, R. (1967). The effect of couple-stresses on the stress concentration around a crack. *International Journal of Solids and Structures, 3*, 69–95.
Suh, H. S., Sun, W. C., & O'Connor, D. T. (2020). A phase field model for cohesive fracture in micropolar continua. *Computer Methods in Applied Mechanics and Engineering, 369*, Article 113181.
Sukumar, N., & Prevost, J. H. (2003). Modelling quasi-static crack growth with the extended finite element method Part I: Computer implementation. *International Journal of Solids and Structures, 40*, 7513–7537.
Sun, C. T., & Jin, Z. (2011). *Fracture mechanics*. Elsevier Science.
Tada, H., Paris, P. C., & Irwin, G. R. (2000). *The stress analysis of cracks handbook*. ASMR Press.
Tarancon, J. E., Vercher, A., Giner, E., & Fuenmayor, F. J. (2009). Enhanced blending elements for XFEM applied to linear elastic fracture mechanics. *International Journal for Numerical Methods in Engineering, 77*, 126–148.
Tian, R., & Wen, L. (2015). Improved XFEM – An extra-dof free, well-conditioning, and interpolating XFEM. *Computer Methods in Applied Mechanics and Engineering, 285*, 639–658.
Trovalusci, P., & Masiani, R. (2003). Non-linear micropolar and classical continua for anisotropic discontinuous materials. *International Journal of Solids and Structures, 40*, 1281–1297.
Trovalusci, P, & Masiani, R. (1999). Material symmetries of micropolar continua equivalent to lattices. *International Journal of Solids and Structures, 36*, 2091–2108.
Tuna, M., Leonetti, L., Trovalusci, P., & Kirca, M. (2020). Explicit' and 'implicit' non-local continuous descriptions for a plate with circular inclusion in tension. *Meccanica, 55*, 927–944.
Tuna, M., & Trovalusci, P. (2020). Scale dependent continuum approaches for discontinuous assemblies: 'Explicit' and 'implicit' non-local models. *Mechanics Research Communication, 103*, Article 103461.
Tuna, M., & Trovalusci, P. (2021). Stress distribution around an elliptic hole in a plate with 'implicit' and 'explicit' non-local models. *Composite Structures, 256*, Article 113003.
Tuna, M., Trovalusci, P., & Fantuzzi, N. (2024). An energy-based fracture criterion for quasi-brittle crack propagation in micropolar continuum: Analytical and numerical study. *International Journal of Engineering Science*.
Wan, J., Yang, D., Chu, X., & Qu, W. (2022). A micropolar peridynamic differential operator and simulation of crack propagation. *Engineering Fracture Mechanics, 269*, Article 108532.
Wen, L. F., Tian, R., Wang, L. X., & Feng, C. (2023). Improved XFEM for multiple crack analysis: Accurate and efficient implementations for stress intensity factors. *Computer Methods in Applied Mechanics and Engineering, 411*, Article 116045.

Yau, J. F., Wang, S. S., & Corten, H. T. (1980). A mixed-mode crack analysis of isotropic solids using conservation laws of elasticity. *Journal of Applied Mechanics, 47*, 335–341.
Yu, H., & Kuna, M. (2021). Interaction integral method for computation of crack parameters *K-T* – A review. *Engineering Fracture Mechanics, 249*, Article 107722.
Yu, H., Sumigawa, T., & Kitamura, T. (2014). A domain independent interaction integral for linear elastic fracture analysis of micropolar materials. *Mechanics of Materials, 74*, 1–13.
Zhou, L., Zhu, S., & Zhu, Z. (2023). Cosserat ordinary state-based peridynamic model and numerical simulation of rock fracture. *Computers and Geotechnics, 155*, Article 105240.